Effective meson-exchange potentials in the SU_6 quark model for NN and YN interactions

Y. Fujiwara,[1] C. Nakamoto,[2,*] and Y. Suzuki[3]
[1]*Department of Physics, Kyoto University, Kyoto 606-01, Japan*
[2]*Graduate School of Science and Technology, Niigata University, Niigata 950-21, Japan*
[3]*Department of Physics, Niigata University, Niigata 950-21, Japan*
(Received 13 June 1996)

We investigate characteristic properties of effective meson-exchange potentials to achieve a simultaneous description of the nucleon-nucleon (NN) and hyperon-nucleon (YN) interactions in the $(3q)$-$(3q)$ resonating-group formulation of the spin-flavor SU_6 quark model. The quark Hamiltonian includes a phenomenological confinement potential of r^2 type, the full Fermi-Breit interaction with explicit quark-mass dependence, and the central, spin-spin, and tensor components of the meson-exchange potentials generated from the scalar and pseudoscalar meson nonet exchanges. A small number of parameters are determined to fit the S- and P-wave NN phase shifts and the low-energy cross-section data for YN scattering. Satisfactory agreement with experiment is obtained, including the NN phase shifts up to $J=4$ partial waves, the deuteron properties, the effective-range parameters, and the total and differential cross sections of the ΛN and ΣN systems. In the intermediate-energy region with $p_{\rm lab} \geqslant$ 400–500 MeV/c, some discrepancies from the one-boson exchange potentials, such as the Nijmegen and Jülich models, are found for the YN scattering observables. In particular, the total nuclear cross sections of $\Sigma^+ p$ elastic scattering show a smooth decreasing behavior in this energy region. In Λp elastic total cross sections, the cusp structure appearing at the ΣN threshold through the one-pion tensor force is influenced by the antisymmetric $LS^{(-)}$ force generated from the Fermi-Breit interaction. [S0556-2813(96)01111-9]

PACS number(s): 13.75.Cs, 12.39.Jh, 13.75.Ev, 24.85.+p

I. INTRODUCTION

In spite of its basic importance in the study of hypernuclei and strangeness physics [1], the hyperon-nucleon (YN) interaction is not well known, in contrast with the nucleon-nucleon (NN) interaction. In the light of quantum chromodynamics (QCD), the NN and YN interactions both originate from rather complicated nonperturbative dynamics of quarks and gluons. Nevertheless the difference between YN and NN interactions has its origin merely in the differences of the flavor degree of freedom. Since the hyperon and the nucleon belong to the same class of the spin-flavor SU_6 supermultiplet $\underline{56}$ [2], one can anticipate that quark models can afford a possible framework to understand the YN interaction on the same basis as the NN interaction.

The composite nature of the nucleon and hyperon is taken into account most straightforwardly in the resonating-group method (RGM). In the simplest RGM formulation [3] for the NN interaction, the nucleon is assumed to be a $(3q)$ cluster described by a product of $(0s)^3$ harmonic oscillator wave functions, the symmetric SU_4 spin-isospin wave function, and the antisymmetric color-singlet wave function. The relative-motion function between the $(3q)$ clusters is determined by solving the integrodifferential equation (RGM equation) which incorporates the nonlocal quark-exchange kernel generated by the effect of antisymmetrization with respect to all six quarks. The Hamiltonian is composed of the nonrelativistic kinetic-energy term and the effective quark-quark (qq) interaction, which is usually built by combining a phenomenological quark-confining potential with a one-gluon exchange potential through the color analog of the Fermi-Breit (FB) interaction. Besides the quark confinement, mesonic effects are most important among the nonperturbative aspects of QCD. It is therefore natural that the application of this framework to the NN system does not give any medium-range attraction [4]. Since the long-range terms of the interaction are particularly dominated by meson-exchange effects, any RGM description in the simple $(3q)$-$(3q)$ model must comprise effective meson-exchange potentials (EMEP) introduced by some appropriate means.

The first realistic quark-model (QM) study of the NN interaction was carried out by supplementing the well-established one-pion exchange potential (OPEP) and phenomenological medium-range potentials of the central and tensor types in the Schrödinger-type equation equivalent to the RGM equation [5]. The most successful calculation of the NN interaction in this kind of approach is the one by Takeuchi, Shimizu, and Yazaki [6], in which the spin-spin and noncentral terms of the OPEP are introduced by assuming that the pions directly couple with quarks in the quark core. An alternative approach is to assume OPEP between quarks in the RGM formalism and to calculate the quark-exchange kernel explicitly [7]. This program was carried out by the Tübingen group in [8,9]. Their approach includes a pseudoscalar (PS) meson exchange between quarks as well as a phenomenological σ-like potential at the baryon level. A complete microscopic calculation incorporating both PS- and σ-meson exchange potentials acting between quarks has recently been undertaken by the Salamanca group [10,11] for the NN interaction and by the Beijing group for the YN and NN interaction [12–14].

*Present address: Research Center for Nuclear Physics, Osaka University, Ibaraki 567, Japan.

In the microscopic approach of the EMEP, two points have to be clarified: (i) What kind of difference does the EMEP produce depending on whether it is calculated at the *quark level* or at the *baryon level* ? (ii) What is the minimum set of mesons indispensably needed ? An advantage of introducing the EMEP at the quark level lies in the stringent relationship of the flavor dependence on various NN or YN channels, as well as of the relative strength between the direct and exchange terms in the RGM treatment. This feature is particularly important when one attempts to describe the NN and YN interactions in a single framework and to minimize the ambiguity of the YN interaction by utilizing the rich knowledge of the NN interaction. The utility of introducing the EMEP must, however, be examined by careful analysis against experiment. In a recent Physical Review Letter [15], we have proposed a possible framework to introduce the EMEP for a simultaneous description of the NN and YN interactions, and have shown some of the main results. Here we will detail this model and its slightly extended version and show more comprehensive results.

In our recent QM study of the NN and YN interactions [16], we have carried out a detailed analysis of the medium-range central attraction required for a simultaneous description of the NN, ΛN, and ΣN interactions. It is found that the YN systems should have much weaker attraction than the NN system and that the needed EMEP which leads to this feature is conveniently generated from the scalar- (S-) meson nonet exchange in the Nijmegen model-F potential [17]. Furthermore, we have shown that, with only two adjustable parameters determined in the NN sector, the model-F meson parameters incorporated into our QM can yield a reasonable reproduction of all the low-energy cross section data of the YN systems [18,19]. This model called RGM-F introduces besides the S-meson nonet only the tensor component generated from the π- and K-meson exchanges, and uses some approximations in evaluating the spin-flavor factors of the quark-exchange RGM kernel. Since the major part of the vector-meson exchange potential is short-ranged and could possibly be considered as an alternative description to the quark-exchange mechanism, no vector-meson exchange is invoked in accordance with the discussion given in [20]. This assumption seems to be plausible in view of the finding that the NN and YN spin-orbit force generated from the FB interaction already has an appropriate strength to reproduce the empirical behavior of the ^3O phase shifts [21]. One of the unsatisfactory points in RGM-F is, however, that the strength of the EMEP has to be chosen differently depending on the spin-flavor exchange symmetry of the two-baryon system. Another problem is that the threshold energy of the ΣN channel is not reproduced well in the $\Lambda N-\Sigma N(I=1/2)$ coupled-channel system. As we will see in this paper, the correct reproduction of the threshold energy is essential for a quantitative description of the coupling features, particularly, the coupling through the antisymmetric spin-orbit ($LS^{(-)}$) force.

In this study we upgrade the EMEP of the RGM-F [18,19] in two respects. One is to calculate the spin-flavor factors exactly at the quark level, and the other is to include the spin-spin terms originating from all the PS mesons. We show that it is possible to reproduce the available NN and YN data simultaneously in the standard $(3q)$-$(3q)$ formulation, if one assumes the full PS- and S-meson nonet exchanges at the quark level and properly introduces the flavor symmetry breaking in the quark sector. An explicit evaluation of quark-exchange kernels for the EMEP sets a strong constraint in characterizing the flavor dependence of each NN and YN channel. The SU_3 relation of the coupling constants emerges as a natural consequence of the SU_6 quark model. For scalar mesons, one of the SU_3 parameters, the $F/(F+D)$ ratio, turns out to take the SU_6 value of purely electric type. This is not always convenient for the detailed reproduction of the existing experimental data for the low-energy YN cross sections. We will avoid this situation in two ways; one is to change the mixing angle of the flavor-singlet and octet scalar mesons, and the other is to employ the same approximation as RGM-F solely for the isoscalar S-mesons, ϵ and S^*. We call these models FSS and RGM-H, respectively. Since predictions of these two models are not much different except for the roles of the $LS^{(-)}$ force in the $\Lambda N-\Sigma N(I=1/2)$ coupled-channel system, we will discuss mainly the result by FSS in this paper. The main difference of the three models, RGM-F, FSS, and RGM-H, is summarized in Table I.

TABLE I. The interaction types and mesons employed in each model. RGM-H deals with ϵ and S^* mesons in an approximate way as in RGM-F.

Model	Interaction type	Mesons
RGM-F	S central	ϵ, S^*, δ, κ
	PS tensor	π, K
FSS, RGM-H	S central	ϵ, S^*, δ, κ
	PS spin-spin	η', η, π, K
	PS tensor	η', η, π, K

In the next section we will formulate the $(3q)$-$(3q)$ RGM incorporating the EMEP at the quark level. Special attention is paid to the evaluation of the spin-flavor factors of the meson-exchange potentials. This serves to clarify the difference between the previous model RGM-F and the two models, FSS and RGM-H. Some simple spin-flavor factors are given in the Appendix. Section III deals with results and discussions. We first discuss the procedure of the parameter search employed in FSS and RGM-H in Sec. III A. The resultant meson parameters are compared with one of the standard one-boson exchange potential (OBEP) models for the NN and YN interactions. Section III B discusses the NN phase-shift behavior with respect to FSS. The deuteron properties and the effective-range parameters of the NN system are discussed in Sec. III C. Sections III D and III E deal with the phase-shift behavior of the $\Sigma^+ p$ and $\Lambda N-\Sigma N(I=1/2)$ systems, respectively. The YN cross sections in the low- and intermediate-energy region are discussed in Sec. III F. The final section is devoted to a summary.

II. FORMULATION

A. $(3q)$-$(3q)$ RGM

The RGM wave function for the $(3q)$-$(3q)$ system can be expressed as

$$\Psi=\sum_{\alpha}\mathcal{A}'\{\phi_\alpha\chi_\alpha(\boldsymbol{R})\}, \tag{2.1}$$

where the channel wave function $\phi_\alpha=\phi^{(\mathrm{orb})}\xi_\alpha^{\mathrm{SF}}\xi^{\mathrm{C}}$ is composed of the orbital part of the internal wave function $\phi^{(\mathrm{orb})}=\phi^{(\mathrm{orb})}(123)\phi^{(\mathrm{orb})}(456)$, the isospin-coupled basis ξ_α^{SF} of the spin-flavor SU_6 wave functions, and the color-singlet wave function $\xi^{\mathrm{C}}=C(123)C(456)$. For $\phi^{(\mathrm{orb})}(123)$ we adopt a simple $(0s)^3$ configuration with a common harmonic oscillator constant b. The center-of-mass (c.m.) motion is eliminated with the use of the usual definition of the c.m. coordinate $\boldsymbol{X}_G=(\boldsymbol{x}_1+\boldsymbol{x}_2+\boldsymbol{x}_3)/3$. Namely, the orbital functions for the $(3q)$ clusters are assumed to be flavor independent and are taken to be the same for all the octet baryons. The isospin-coupled basis ξ_α^{SF} incorporates the generalized Pauli principle, $(-1)^{L+S}\mathcal{P}=1$, with respect to the eigenvalue $\mathcal{P}$ of the flavor-exchange operator $P_0^{\mathrm{F}}=P_{14}^{\mathrm{F}}P_{25}^{\mathrm{F}}P_{36}^{\mathrm{F}}$ namely,

$$P_0^{\mathrm{F}}\xi_\alpha^{\mathrm{SF}}=\mathcal{P}\xi_\alpha^{\mathrm{SF}}, \tag{2.2}$$

where the subscript α specifies a set of quantum numbers of the channel wave function, $\alpha=[1/2(11)a_1,1/2(11)a_2]\,\mathrm{SS}_zYII_z;\mathcal{P}$. Here $1/2(11)a$ denotes the spin, the SU_3 quantum number in the Elliott notation $(\lambda\mu)$, and the flavor label YI of the octet baryons, respectively. For example, $YI=1(1/2)$ for N, 00 for Λ, and 01 for Σ. The explicit expression of ξ_α^{SF} is given in Eqs. (2.5) – (2.8) of [16]. The antisymmetrization operator $\mathcal{A}'$ in Eq. (2.1) makes Ψ totally antisymmetric under the exchange of any quark pairs and can be reduced to the form $\mathcal{A}'\to(1/2)(1-9P_{36})(1-P_0)$ with $P_0=P_{14}P_{25}P_{36}$ being the core-exchange operator of the two $(3q)$ clusters.

The QM Hamiltonian consists of the nonrelativistic kinetic-energy term, the quadratic confinement potential, the full FB interaction with explicit quark-mass dependence, and the S- and PS-meson exchange potentials acting between quarks:

$$H=\sum_{i=1}^{6}\left(m_i+\frac{\boldsymbol{p}_i^2}{2m_i}\right)+\sum_{i<j}^{6}\left(U_{ij}^{\mathrm{Cf}}+U_{ij}^{\mathrm{FB}}+\sum_\beta U_{ij}^{\mathrm{S}\beta}+\sum_\beta U_{ij}^{\mathrm{PS}\beta}\right). \tag{2.3}$$

Here $U_{ij}^{\mathrm{Cf}}=-(\lambda_i^{\mathrm{C}}\cdot\lambda_j^{\mathrm{C}})a_c r^2$ with $r=|\boldsymbol{r}|=|\boldsymbol{x}_i-\boldsymbol{x}_j|$ is the confinement potential of quadratic power law, which is known to give a vanishing contribution to the interaction in the present formalism. The qq FB interaction U_{ij}^{FB} is composed of the following pieces:

$$U_{ij}^{\mathrm{FB}}=U_{ij}^{\mathrm{CC}}+U_{ij}^{\mathrm{MC}}+U_{ij}^{\mathrm{GC}}+U_{ij}^{\mathrm{sLS}}+U_{ij}^{\mathrm{aLS}}+U_{ij}^{\mathrm{T}}, \tag{2.4}$$

where the superscript CC stands for the color-Coulombic or $(\lambda_i^{\mathrm{C}}\cdot\lambda_j^{\mathrm{C}})/r$ piece, MC for the momentum-dependent Breit retardation term or $(\lambda_i^{\mathrm{C}}\cdot\lambda_j^{\mathrm{C}})\{(\boldsymbol{p}_i\cdot\boldsymbol{p}_j)+\boldsymbol{r}(\boldsymbol{r}\cdot\boldsymbol{p}_i)\cdot\boldsymbol{p}_j/r^2\}/(m_im_jr)$ piece, GC for the combined color-δ and color-magnetic or $(\lambda_i^{\mathrm{C}}\cdot\lambda_j^{\mathrm{C}})\ \{1/(2m_i^2)+1/(2m_j^2)+2/(3m_im_j)\times(\boldsymbol{\sigma}_i\cdot\boldsymbol{\sigma}_j)\}\delta(\boldsymbol{r})$ piece, (sLS) for the symmetric LS, (aLS) for the antisymmetric LS, and (T) for the tensor term. For the S- and PS-meson exchange potentials, we adopt the lowest-order central, spin-spin, and tensor terms originating from the flavor-singlet and octet mesons labeled β:

$$U_{ij}^{\mathrm{S}\beta}=-w_{ij}^{\mathrm{S}\beta}m_\beta Y(x),\quad U_{ij}^{\mathrm{PS}\beta}=w_{ij}^{\mathrm{PS}\beta}\left(\frac{m_\beta}{m_{\pi^+}}\right)^2\frac{m_\beta}{3}\left\{(\boldsymbol{\sigma}_i\cdot\boldsymbol{\sigma}_j)\left[Y(x)-c_\delta\frac{4\pi}{{m_\beta}^3}\delta(\boldsymbol{r})\right]+S_{12}\left[Z(x)-\frac{4\pi}{{m_\beta}^3}\delta(\boldsymbol{r})\right]\right\}, \tag{2.5}$$

where $w_{ij}^{\mathrm{S}\beta}$ and $w_{ij}^{\mathrm{PS}\beta}$ are appropriate flavor operators and c_δ is a reduction factor, both of which will be discussed in detail in the next subsection. Furthermore, $Y(x)=e^{-x}/x$, $Z(x)=(1+3/x+3/x^2)Y(x)$ with $x=m_\beta|\boldsymbol{r}|$, and $S_{12}=3(\boldsymbol{\sigma}_i\cdot\hat{\mathbf{r}})(\boldsymbol{\sigma}_j\cdot\hat{\mathbf{r}})-(\boldsymbol{\sigma}_i\cdot\boldsymbol{\sigma}_j)$ is the tensor operator.

The RGM equation is derived from the variational principle

$$\langle\delta\Psi|E-H|\Psi\rangle=0, \tag{2.6}$$

with respect to the relative wave function $\chi_\alpha(\boldsymbol{R})$ of Eq. (2.1). The standard procedure yields

$$\left[\varepsilon_\alpha+\frac{\hbar^2}{2\mu_\alpha}\left(\frac{\partial}{\partial\boldsymbol{R}}\right)^2-\sum_\beta V_{\alpha D}^{(\mathrm{CN})\beta}(\boldsymbol{R})-\sum_\beta V_{\alpha D}^{(\mathrm{SS})\beta}(\boldsymbol{R})-\sum_\beta V_{\alpha D}^{(\mathrm{TN})\beta}(\boldsymbol{R})S_{12}\right]\chi_\alpha(\boldsymbol{R})$$
$$=\sum_{\alpha'}\int d\boldsymbol{R}'\left[\sum_\Omega\mathcal{M}_{\alpha\alpha'}^{(\Omega)}(\boldsymbol{R},\boldsymbol{R}')-\varepsilon_\alpha\mathcal{M}_{\alpha\alpha'}^{\mathrm{N}}(\boldsymbol{R},\boldsymbol{R}')\right]\chi_{\alpha'}(\boldsymbol{R}'), \tag{2.7}$$

where S_{12} is now the tensor operator at the baryon level. The relative energy ε_α in the channel α is defined by subtracting the internal energies of the clusters from the total energy E. The quark-exchange kernels $\mathcal{M}_{\alpha\alpha'}^{(\Omega)}(\boldsymbol{R},\boldsymbol{R}')$ on the right-hand side of Eq. (2.7) include a sum over $\Omega=\mathrm{K}$ for the kinetic-energy term, CC, MC, GC, sLS, aLS, T for each piece of the FB interaction in Eq. (2.4), as well as CN for the central term of the S-meson exchange, SS for the spin-spin term of the PS-meson exchange, and TN for the tensor term of the PS-meson exchange corresponding to Eq. (2.5). The direct potentials $V_{\alpha D}^{(\Omega)\beta}(\boldsymbol{R})$ of Eq. (2.7) are given by

$$V_{\alpha D}^{(\mathrm{CN})\beta}(\boldsymbol{R})=-(X_{0D_+}^{(\mathrm{CN})\beta})_{\alpha\alpha}m_\beta Y_{\alpha_0}(x),\quad V_{\alpha D}^{(\mathrm{SS})\beta}(\boldsymbol{R})=(X_{0D_+}^{(\mathrm{SS})\beta})_{\alpha\alpha}\left(\frac{m_\beta}{m_{\pi^+}}\right)^2\frac{m_\beta}{3}[Y_{\alpha_0}(x)-c_\delta D_{\alpha_0}(x)],$$

$$V_{\alpha D}^{(\mathrm{TN})\beta}(\boldsymbol{R})=(X_{0D_+}^{(\mathrm{TN})\beta})_{\alpha\alpha}\left(\frac{m_\beta}{m_{\pi^+}}\right)^2\frac{m_\beta}{3}[Z_{\alpha_0}(x)-D_{\alpha_0}(x)], \tag{2.8}$$

where $Y_{\alpha_0}(x)$, $Z_{\alpha_0}(x)$, and $D_{\alpha_0}(x)$ with $x=m_\beta|\boldsymbol{R}|$ and $\alpha_0=(m_\beta b)^2/3$ are the standard OBEP functions with a Gaussian form factor $F(\boldsymbol{q}^2)=\exp\{-(b\boldsymbol{q})^2/6\}$, and their forms are given in Eq. (A2) of [18]. The spin-flavor-color factors $(X_{0D_+}^{(\Omega)\beta})_{\alpha\alpha}$ in Eq. (2.8) are defined through more general n-quark-exchange factors depending on α-α' channels:

$$\begin{Bmatrix} X_{n\mathcal{T}}^{(\mathrm{CN})\beta} \\ X_{n\mathcal{T}}^{(\mathrm{SS})\beta} \end{Bmatrix}_{\alpha\alpha'}=C_n\langle z_n\xi_\alpha|\sum_{(i,j)\in\mathcal{T}}\begin{Bmatrix} w_{ij}^{\mathrm{S}\beta} \\ w_{ij}^{\mathrm{PS}\beta}(\boldsymbol{\sigma}_i\cdot\boldsymbol{\sigma}_j)\end{Bmatrix}|\xi_{\alpha'}\rangle,$$

$$(X_{n\mathcal{T}}^{(\mathrm{TN})\beta})_{\alpha\alpha'}=C_n\langle z_n\xi_\alpha\|\sum_{(i,j)\in\mathcal{T}}w_{ij}^{\mathrm{PS}\beta}[\boldsymbol{\sigma}_i\times\boldsymbol{\sigma}_j]^{(2)}\|\xi_{\alpha'}\rangle\langle 1\|[\boldsymbol{\sigma}_{B_1}\times\boldsymbol{\sigma}_{B_2}]^{(2)}\|1\rangle^{-1}. \tag{2.9}$$

Here $\xi_\alpha=\xi_\alpha^{\mathrm{SF}}\xi^{\mathrm{C}}$, $\boldsymbol{\sigma}_B$ is the baryon spin operator, and $C_0=1$, $C_1=-9$, $z_0=1$, and $z_1=P_{36}^{\mathrm{SF}}P_{36}^{\mathrm{C}}$ come from $\mathcal{A}'$. The subscript $\mathcal{T}$ specifies five different interaction types, E, S, S', D_+, and D_- [22,23]. The internal-energy factor with $\mathcal{T}=E$ and the direct-potential factor with $\mathcal{T}=D_+$ are only possible for the direct term with $n=0$.

In Eq. (2.3), we should note that the total kinetic-energy operator is not subtracted from the full Hamiltonian. This is purposely done since Galilean invariance is not respected in our formalism. The appearance of the Galilean noninvariant terms like the momentum-dependent retardation term U_{ij}^{MC} is a direct consequence of the more strict Lorentz invariance at the relativistic level, and their RGM kernel should be explicitly evaluated in the total c.m. system [16]. Even if one includes the U_{ij}^{MC} term and takes account of its contribution to the relative kinetic-energy term, the calculated reduced mass of the ΣN system is degenerate with that of the ΛN system. This is one of the limitations of the nonrelativistic quark model, in which the inertia masses (of Σ and Λ in the present case) are not always reproduced correctly. In order to use the correct reduced masses in the coupled RGM equation, we make the following replacement only for the exchange kernels $\mathcal{M}_{\alpha\alpha'}^{(\mathrm{K})}(\boldsymbol{R},\boldsymbol{R}')$ and $\mathcal{M}_{\alpha\alpha'}^{(\mathrm{MC})}(\boldsymbol{R},\boldsymbol{R}')$ [19]:

$$\mathcal{M}_{\alpha\alpha'}^{(\Omega)}(\boldsymbol{R},\boldsymbol{R}')\rightarrow\widetilde{\mathcal{M}}_{\alpha\alpha'}^{(\Omega)}(\boldsymbol{R},\boldsymbol{R}')=\sqrt{\frac{\mu_\alpha\mu_{\alpha'}}{\mu_\alpha^{\mathrm{expt}}\mu_{\alpha'}^{\mathrm{expt}}}}\mathcal{M}_{\alpha\alpha'}^{(\Omega)}(\boldsymbol{R},\boldsymbol{R}')$$

$$\text{for } \Omega=\mathrm{K} \text{ and } \mathrm{MC}. \tag{2.10}$$

This prescription does not spoil the Pauli principle in the single-channel system like NN and Σ^+p [16]. In the ΛN-$\Sigma N(I=1/2)$ coupled-channel system, this procedure causes only a slight inaccuracy with respect to the treatment of the Pauli principle except for the $^1S_0$ state, in which a complete Pauli-forbidden state with $(0s)^6$ configuration exists in the spin-flavor SU_6 coupling $1/2\,(11)\times 1/2\,(11)\rightarrow 0\,(11)_s$. The treatment in this case is carefully spelled out in [19]. With this procedure we can employ the empirical reduced mass without impairing the major part of the Pauli principle, thus avoiding the kinematical ambiguity which influences the subtle features of the $\Lambda N-\Sigma N$ coupling.

Another nice property of the present RGM formalism is that the internal-energy contribution is already subtracted in the exchange kernel. Namely, $\mathcal{M}_{\alpha\alpha'}^{(\Omega)}(\boldsymbol{R},\boldsymbol{R}')$ for the central components $\Omega=$K, CC, MC, GC, CN, and SS is defined through its corresponding original exchange kernel $\mathcal{M}_{\alpha\alpha'}^{(\Omega)\mathrm{exch}}(\boldsymbol{R},\boldsymbol{R}')$:

$$\mathcal{M}_{\alpha\alpha'}^{(\Omega)}(\boldsymbol{R},\boldsymbol{R}')=\mathcal{M}_{\alpha\alpha'}^{(\Omega)\mathrm{exch}}(\boldsymbol{R},\boldsymbol{R}')-(E_{a_1}^{(\Omega)}+E_{a_2}^{(\Omega)})\mathcal{M}_{\alpha\alpha'}^{\mathrm{N}}(\boldsymbol{R},\boldsymbol{R}'), \tag{2.11}$$

where $E_a^{(\Omega)}$ denotes the Ω-term contribution to the internal energy of the octet baryon specified by the flavor label a. Owing to this subtraction, the mass term of the kinetic-energy operator in Eq. (2.3) as well as the confinement potential with $\Omega=Cf$ exactly cancels out between the first and the second terms on the right-hand side of Eq. (2.11). We consider this feature one of the advantages of the RGM formalism, because the present quark model is independent of the strength of the confinement potential and is insensitive to the details of the confinement phenomenology.

The scattering matrix $S_{\alpha\alpha'}$ is calculated by solving the coupled-channel RGM equation of Eq. (2.7) by a variational technique developed by Kamimura [24]. It can be expressed as

$$S_{\alpha\alpha'}=\eta_{\alpha\alpha'}e^{2i\delta_{\alpha\alpha'}}, \tag{2.12}$$

where $\eta_{\alpha\alpha'}=|S_{\alpha\alpha'}|$ are the reflection and transmission coefficients for $\alpha=\alpha'$ and $\alpha\neq\alpha'$, respectively. The Coulomb force is entirely neglected in the $\Lambda N-\Sigma N(I=1/2)$ coupled-channel system when the Λp channel is an incident channel. The scattering amplitudes in the particle basis are then given by

$$\langle \Lambda p|M|\Lambda p\rangle = \langle \Lambda N|M(I=\tfrac{1}{2})|\Lambda N\rangle,$$

$$\langle \Sigma^0 p|M|\Lambda p\rangle = -\frac{1}{\sqrt{3}}\langle \Sigma N|M(I=\tfrac{1}{2})|\Lambda N\rangle,$$

$$\langle \Sigma^+ n|M|\Lambda p\rangle = \sqrt{\frac{2}{3}}\langle \Sigma N|M(I=\tfrac{1}{2})|\Lambda N\rangle. \quad (2.13)$$

If the $\Sigma^- p$ channel is an incident channel, we include the Coulomb attraction in the $\Sigma N(I=1/2)$ and $\Sigma N(I=3/2)$ channels separately by neglecting the isospin symmetry breaking. Namely, we first calculate the scattering matrices of the $\Sigma N(I=1/2)-\Lambda N$ and $\Sigma N(I=3/2)$ systems by assuming the Coulomb attraction for the $\Sigma^- p$ system. The scattering amplitudes from $\Sigma^- p$ to $\Sigma^- p$, $\Sigma^0 n$, and Λn channels are then generated by employing the isospin relations:

$$\langle \Sigma^- p|M|\Sigma^- p\rangle = \frac{1}{3}\{\langle \Sigma N|M(I=\tfrac{3}{2})|\Sigma N\rangle + 2\langle \Sigma N|M(I=\tfrac{1}{2})|\Sigma N\rangle\},$$

$$\langle \Sigma^0 n|M|\Sigma^- p\rangle = \frac{\sqrt{2}}{3}\{\langle \Sigma N|M(I=\tfrac{3}{2})|\Sigma N\rangle - \langle \Sigma N|M(I=\tfrac{1}{2})|\Sigma N\rangle\},$$

$$\langle \Lambda n|M|\Sigma^- p\rangle = -\sqrt{\frac{2}{3}}\langle \Lambda N|M(I=\tfrac{1}{2})|\Sigma N\rangle. \quad (2.14)$$

The spin-flavor-color factors of the exchange Coulomb kernel are explicitly calculated only for the pp system and they are given in the Appendix. For the other systems they are assumed to be proportional to the factors of the exchange normalization kernel, as in Eq. (A9) of [18]. In this approximate treatment of the Coulomb force, at most four channels specified by ${}^{2S+1}L_J$ couple for a given total angular momentum J and parity. The ${}^1L_J$ and ${}^3L_J$ partial waves with $J=L$ couple to each other by the antisymmetric $LS^{(-)}$ force, and its coupling is incorporated in the YN systems.

B. Effective meson-exchange potentials

The flavor operators $w_{ij}^{S\beta}$ and $w_{ij}^{PS\beta}$ in Eq. (2.5) are generated from the SU_3-scalar combination of the extended Gell-Mann matrix, $\lambda_{(00)}=-1/\sqrt{6}$ and $\lambda_{(11)\alpha}=(1/2)\{\lambda^1,\lambda^2,\ldots,\lambda^8\}$:

$$w_{ij}^{(\lambda\lambda)} = 4f_0^2\sum_\alpha \lambda_{(\lambda\lambda)\alpha}^\dagger(i)\lambda_{(\lambda\lambda)\alpha}(j) = f_0^2\begin{cases}2/3 \\ (\lambda_i\cdot\lambda_j)\end{cases} \text{ for } (\lambda\lambda)=\begin{cases}(00), \\ (11).\end{cases} \quad (2.15)$$

Here $(\lambda_i\cdot\lambda_j)=\Sigma_{c=1}^8\lambda_i^c\lambda_j^c$ is the Casimir operator in the usual notation. The flavor index β is assigned to the SU_3 label $(\lambda\lambda)=(00)$ or (11) corresponding to the flavor-singlet or octet meson. The spin-flavor-color factors, $X_{n\mathcal{T}}^{(\Omega)(00)}$ and $X_{n\mathcal{T}}^{(\Omega)(11)}$ ($\Omega=$CN, SS, and TN), defined through Eq. (2.9) are easily calculated by using the properties of the exchange operators in the spin and flavor SU_3 spaces, and are expressed by the SU_6 unit vectors, $e_{(\lambda\lambda)}^e$ and $e_{(\lambda\lambda)}^m$, for the SU_6 coupling $[3]\times[21^4]\to[41^5]\sim[3]$. (See [25,26] for the operator representation technique of the spin-flavor factors.) The D_+ factors for the direct term with $n=0$ are particularly simple since one only needs to replace the quark operator $\lambda_{(\lambda\lambda)}(i)$ in Eq. (2.15) with the SU_6 unit vectors $(1/6)e_{(\lambda\lambda)}^e$ and $(1/6)e_{(\lambda\lambda)}^m$ of each $(3q)$ cluster, corresponding to the spin-involved and noninvolved cases, respectively:

$$X_{0D_+}^{(CN)(\lambda\lambda)} = f_0^2 e_{(\lambda\lambda)}^{e\dagger}e_{(\lambda\lambda)}^e, \quad X_{0D_+}^{(TN)(\lambda\lambda)} = f_0^2 e_{(\lambda\lambda)}^{m\dagger}e_{(\lambda\lambda)}^m, \quad (2.16)$$

where a simplified notation,

$$e_{(\lambda\lambda)}^{\tau\dagger}e_{(\lambda\lambda)}^{\tau} \equiv \Sigma_\alpha e_{(\lambda\lambda)\alpha}^{\tau\dagger}(B_1)e_{(\lambda\lambda)\alpha}^{\tau}(B_2) \quad (\tau=e \text{ or } m),$$

is employed. From Eq. (2.16) one can immediately see that the SU_3 relations are naturally incorporated in the present formalism. The tensor and spin-spin factors with $n=0$ are related to each other by

$$X_{0D_+}^{(SS)\beta} = X_{0D_+}^{(TN)\beta}(\boldsymbol{\sigma}_{B_1}\cdot\boldsymbol{\sigma}_{B_2}). \quad (2.17)$$

This implies that we only need to calculate spin-flavor-color factors of the tensor term for PS mesons as far as the direct term is concerned. Equation (A1) of the Appendix lists the spin-flavor-color factors for the choice of $w_{ij}^{(00)}=1$ and $w_{ij}^{(11)}=(\lambda_i\cdot\lambda_j)$, where the trivial numerical factors $(2/3)f_0^2$ and f_0^2 of Eq. (2.15) are omitted.

In the SU_3 approximation of the EMEP the coupling constant f_0 at the quark level is chosen for each of the four combinations; S-meson singlet and octet, and PS-meson singlet and octet. These coupling constants are most transparently expressed in terms of the SU_3 coupling constants at the baryon level, f_1^S, f_8^S, f_1^{PS}, and f_8^{PS}, which appear in the vertex Lagrangian functions for the baryon-baryon-meson couplings. The spin-flavor-color factors of Eq. (2.16) for the direct terms are factorized into the desired form by taking the matrix elements of the SU_6 unit vectors with respect to the flavor wave functions of the octet baryons. By employing $e_{(00)}^e=-\sqrt{6}$, $e_{(00)}^m=-\sqrt{2/3}$, and the SU_3 standard matrix elements $e_{NN\delta}^e=1$, $e_{NN\pi}^m=5/3$ (see Table I of [25]), we easily find that

$$(f_0)^{S(00)}=\frac{1}{\sqrt{6}}f_1^S, \quad (f_0)^{S(11)}=f_8^S,$$

$$(f_0)^{PS(00)}=\sqrt{\frac{3}{2}}f_1^{PS}, \quad (f_0)^{PS(11)}=\frac{3}{5}f_8^{PS}. \quad (2.18)$$

We also introduce the singlet-octet meson mixing for the isoscalar mesons. As is discussed in [16], this process is essential to reproduce the necessary flavor dependence of the central attraction generated from the ϵ-meson exchange potentials for NN and YN channels. We introduce this mixing in Eq. (2.15) by employing a simple rotation

$$\lambda_{(00)} \rightarrow \lambda_{(00)}\cos\theta - \lambda_{(11)000}\sin\theta,$$

$$\lambda_{(11)000} \rightarrow \lambda_{(00)}\sin\theta + \lambda_{(11)000}\cos\theta. \tag{2.19}$$

One needs to introduce two mixing angles, $\theta_{\rm S}$ and $\theta_{\rm PS}$, for S and PS mesons, respectively. Furthermore, we decompose nonisoscalar components of $w_{ij}^{(11)}$ in Eq. (2.15) into isovector ($I=1$) and $I=1/2$ components, since the isovector mesons and the strange mesons usually have different masses. With all these relations, the flavor operators $w_{ij}^{{\rm S}\beta}$ and $w_{ij}^{{\rm PS}\beta}$ in Eq. (2.5) are assumed to be

$$w_{ij}^{\epsilon} = \left(\frac{1}{3}f_1^{\rm S}\cos\theta_{\rm S} + f_8^{\rm S}\sin\theta_{\rm S}\lambda_i^8\right) \times \left(\frac{1}{3}f_1^{\rm S}\cos\theta_{\rm S} + f_8^{\rm S}\sin\theta_{\rm S}\lambda_j^8\right),$$

$$w_{ij}^{\rm S*} = \left(-\frac{1}{3}f_1^{\rm S}\sin\theta_{\rm S} + f_8^{\rm S}\cos\theta_{\rm S}\lambda_i^8\right) \times \left(-\frac{1}{3}f_1^{\rm S}\sin\theta_{\rm S} + f_8^{\rm S}\cos\theta_{\rm S}\lambda_j^8\right),$$

$$w_{ij}^{\delta} = (f_8^{\rm S})^2\sum_{c=1}^{3}\lambda_i^c\lambda_j^c, \quad w_{ij}^{\kappa} = (f_8^{\rm S})^2\sum_{c=4}^{7}\lambda_i^c\lambda_j^c \tag{2.20}$$

for S mesons and

$$w_{ij}^{\eta'} = \left(f_1^{\rm PS}\cos\theta_{\rm PS} + \frac{3}{5}f_8^{\rm PS}\sin\theta_{\rm PS}\lambda_i^8\right) \times \left(f_1^{\rm PS}\cos\theta_{\rm PS} + \frac{3}{5}f_8^{\rm PS}\sin\theta_{\rm PS}\lambda_j^8\right),$$

$$w_{ij}^{\eta} = \left(-f_1^{\rm PS}\sin\theta_{\rm PS} + \frac{3}{5}f_8^{\rm PS}\cos\theta_{\rm PS}\lambda_i^8\right) \times \left(-f_1^{\rm PS}\sin\theta_{\rm PS} + \frac{3}{5}f_8^{\rm PS}\cos\theta_{\rm PS}\lambda_j^8\right),$$

$$w_{ij}^{\pi} = \left(\frac{3}{5}f_8^{\rm PS}\right)^2\sum_{c=1}^{3}\lambda_i^c\lambda_j^c, \quad w_{ij}^{K} = \left(\frac{3}{5}f_8^{\rm PS}\right)^2\sum_{c=4}^{7}\lambda_i^c\lambda_j^c, \tag{2.21}$$

for PS mesons. The isoscalar spin-flavor factors in Eq. (2.8) are given by

$$X_{0D_+}^{({\rm CN})\epsilon} = (f_1^{\rm S}\cos\theta_{\rm S} + f_8^{\rm S}\sin\theta_{\rm S}e_{(11)000}^{e\dagger}) \times (f_1^{\rm S}\cos\theta_{\rm S} + f_8^{\rm S}\sin\theta_{\rm S}e_{(11)000}^{e}),$$

$$X_{0D_+}^{({\rm TN})\eta'} = \left(f_1^{\rm PS}\cos\theta_{\rm PS} + \frac{3}{5}f_8^{\rm PS}\sin\theta_{\rm PS}e_{(11)000}^{m\dagger}\right) \times \left(f_1^{\rm PS}\cos\theta_{\rm PS} + \frac{3}{5}f_8^{\rm PS}\sin\theta_{\rm PS}e_{(11)000}^{m}\right). \tag{2.22}$$

The factor for $X_{0D_+}^{({\rm CN})S*}$ ($X_{0D_+}^{({\rm TN})\eta}$) is obtained by replacing $\theta_{\rm S}$ ($\theta_{\rm PS}$) with $\theta_{\rm S}-\pi/2$ ($\theta_{\rm PS}-\pi/2$) in the above expressions. Those for the isovector and $I=1/2$ mesons are obtained by the corresponding partial sum over α of $e_{(11)\alpha}^{\tau}$ in Eq. (2.16).

We here remark on the characteristic features of the EMEP in the present model. In RGM-F [18,19] we first assumed pure flavor-singlet mesons to avoid the calculation of the spin-flavor-color factors, and then introduced the explicit flavor dependence of the Nijmegen model-F potential for the products of the coupling constants. This procedure is possible because the direct potentials of Eq. (2.8) have the same structure as the standard OBEP with Gaussian form factors if $X_{0D_+}^{(\Omega)\beta}$ are replaced with the products of baryon-meson coupling constants. The result of Eqs. (2.16) and (2.22) implies that a similar correspondence to the OBEP models is still possible even if we start from an original flavor-dependent qq interaction as in Eqs. (2.20) and (2.21). The parameters, $f_1^{\rm S}$, $f_8^{\rm S}$, $\theta_{\rm S}$, and $f_1^{\rm PS}$, $f_8^{\rm PS}$, $\theta_{\rm PS}$, at the baryon level can be used to specify the SU_3 parameters of the original qq interaction. We note that the present model has the short-range part arising from the exchange kernel. This short-range effect of the EMEP is of purely microscopic origin, and is not incorporated in OBEP models. Furthermore, another SU_3 parameter, $\alpha = f_8^F/(f_8^D + f_8^F)$, is no longer a free parameter in the present framework, but takes the pure SU_6 values, $\alpha=1$ (for S mesons) and $\alpha=2/5$ (for PS mesons), as is seen from Eq. (2.16) with $(\lambda\lambda)=(11)$. Namely, the $e_{(11)}^{e\dagger}e_{(11)}^{e}$ dependence in $X_{0D_+}^{({\rm CN})(11)}$ implies pure electric-type coupling for the scalar mesons, while $e_{(11)}^{m\dagger}e_{(11)}^{m}$ in $X_{0D_+}^{({\rm SS})(11)}$ and $X_{0D_+}^{({\rm TN})(11)}$ implies pure magnetic-type coupling for the PS mesons. As we will see in the next section, this turns out to be a rather severe restriction of the SU_6 quark model.

Another essential difference between RGM-F and the present improved models lies in the internal energy contribution from the EMEP. In RGM-F the approximation for the products of the coupling constants is made after the internal-energy subtraction of Eq. (2.11) is carried out. Thus the Λ and Σ mass difference, $\Delta E_{\Lambda-\Sigma}^{M} = E_{\Sigma}^{M} - E_{\Lambda}^{M}$, has vanishing contribution from the EMEP. On the other hand, the value of $\Delta E_{\Lambda-\Sigma}^{M}$ can be calculated by using $X_{0E}^{({\rm CN})\beta}$ and $X_{0E}^{({\rm SS})\beta}$ in the present framework. The contribution of the EMEP to $\Delta E_{\Lambda-\Sigma}^{M}$ is divided between the S-meson and PS-meson parts; $\Delta E_{\Lambda-\Sigma}^{M} = \Delta E_{\Lambda-\Sigma}^{\rm CN} + \Delta E_{\Lambda-\Sigma}^{\rm SS}$ They are given by

$$\Delta E_{\Lambda-\Sigma}^{\rm CN} = (f_8^{\rm S})^2\{-4m_{\delta}Y_{\alpha_E^{\delta}}(0) + 4m_{\kappa}Y_{\alpha_E^{\kappa}}(0)\},$$

$$\Delta E^{\rm SS}_{\Lambda-\Sigma}=\Delta W^{\rm SS}_{\Lambda-\Sigma}(\theta_{\rm PS})\left(\frac{m_{\eta'}}{m_{\pi^+}}\right)^2\frac{m_{\eta'}}{3}[Y_{\alpha^{\eta'}_E}(0)-c_\delta D_{\alpha^{\eta'}_E}(0)]+\Delta W^{\rm SS}_{\Lambda-\Sigma}(\theta_{\rm PS}-\pi/2)\left(\frac{m_\eta}{m_{\pi^+}}\right)^2\frac{m_\eta}{3}[Y_{\alpha^{\eta}_E}(0)-c_\delta D_{\alpha^{\eta}_E}(0)]$$
$$+\left(\frac{3}{5}f_8^{\rm PS}\right)^2\left\{-8\left(\frac{m_\pi}{m_{\pi^+}}\right)^2\frac{m_\pi}{3}[Y_{\alpha^{\pi}_E}(0)-c_\delta D_{\alpha^{\pi}_E}(0)]+4\left(\frac{m_K}{m_{\pi^+}}\right)^2\frac{m_K}{3}[Y_{\alpha^{K}_E}(0)-c_\delta D_{\alpha^{K}_E}(0)]\right\}, \tag{2.23}$$

where $\alpha^\beta_E=(m_\beta b)^2/2$ and $\Delta W^{\rm SS}_{\Lambda-\Sigma}(\theta)$ is defined by

$$\Delta W^{\rm SS}_{\Lambda-\Sigma}(\theta)=4\left(\frac{3}{5}f_8^{\rm PS}\right)\sin\theta\left(\sqrt{3}f_1^{\rm PS}\cos\theta+\frac{3}{5}f_8^{\rm PS}\sin\theta\right). \tag{2.24}$$

Before discussing the contribution of the EMEP to the $\Lambda-\Sigma$ mass difference, we discuss the reduction factor c_δ introduced in the spin-spin term of the PS-meson EMEP. [See Eq. (2.5).] The δ-function-type contact term is usually ignored in OBEP for point nucleons by an *ad hoc* procedure. The inclusion of the term induces rather vigorous repulsive behavior in the short-range region of the NN interaction. (See [7,27] for OPEP.) We include η and η' mesons to make it possible to choose a unique set of the scalar-meson coupling constants for the flavor-symmetric and antisymmetric configurations of the NN and YN systems. The full inclusion of this term with $c_\delta=1$ strongly hinders the role of η and η' mesons, and makes it very difficult to find a simultaneous fit to the S-wave and P-wave NN phase shifts. Without this term the pion gives a negative contribution to the $\Lambda-\Sigma$ mass difference [see Eq. (2.23)], and the reproduction of the ΣN threshold energy becomes very hard in the $\Lambda N-\Sigma N(I=1/2)$ coupled-channel system. We therefore assume a single reduction factor c_δ around 0.3–0.4 common to all the NN and YN channels.

Table II shows the contributions of the various terms to the $\Lambda-\Sigma$ mass difference for the models, RGM-F, FSS, and RGM-H. The explicit parameter values of FSS and RGM-H will be given in the next section, after the difference of the models is clarified. We find that the mesonic contributions are by no means small, and should be properly taken into account in the RGM formalism. The pion does not make a dominant contribution partly because of the reduction factor c_δ. There is a large cancellation among the contributions of various mesons. As Eq. (2.23) shows, the isoscalar S mesons do not contribute to $\Delta E^{\rm CN}_{\Lambda-\Sigma}$, while δ and κ contributions largely cancel, as well as η and η' contributions. The cancellation between δ and κ becomes perfect when $m_\delta=m_\kappa$. As a result, the pion contribution might be a good estimate for the total meson contribution. However, this is very sensitive to the particular values of parameters such as $f_8^{\rm S}$, m_κ, and m_δ. Since it is very important to reproduce the correct threshold energy in the $\Lambda-\Sigma(I=1/2)$ coupled-channel problem, we will make the parameter search under the constraint that the correct mass difference $\Delta E_{\Lambda-\Sigma}=77.49$ MeV is always reproduced.

TABLE II. Quark and meson contributions to $\Lambda-\Sigma$ mass difference ($\Delta E_{\Lambda\text{-}\Sigma}$) in MeV for RGM-F, FSS, and RGM-H. The mass ratio of strange to up-down quarks, $\lambda=(m_s/m_{ud})=1.25$, 1.526, and 1.490, are employed to calculate the quark contribution in RGM-F, FSS, and RGM-H, respectively. See Table III for the other parameters.

β	RGM-F	FSS	RGM-H
Quark	39	67	43
δ	0	−100	−52
κ	0	76	58
η'	−	−13	−8
η	−	15	13
π	−	25	15
K	−	7	8
Total	39	77	77

So far we have discussed only the mass difference of the octet baryons, but not their absolute values. The absolute masses are not reliably calculated because they strongly depend on the strength of the confinement potential a_c. The nucleon mass can be fitted with $a_c=95.61$ MeV fm^{-2} in FSS, and then the Λ, Σ, and Ξ rest masses are calculated to be 1158, 1236, and 1399 MeV, respectively. Although these values are a little too large compared to the empirical ones, the discrepancies do not affect the QM interaction since the cluster internal energies are already subtracted. A similar evaluation in RGM-H yields $a_c=56.82$ MeV fm^{-2}, and 1103, 1180, and 1344 MeV for the Λ, Σ, and Ξ masses, respectively.

We have also examined the EMEP contribution to the N and Δ mass difference, $\Delta E_{N-\Delta}=E_\Delta-E_N$. Only the nonstrange mesons contribute to this quantity and the δ contribution is partly canceled with the additive PS-meson contributions. This cancellation is also very sensitive to the particular values of the meson parameters, and our $\Delta E_{N-\Delta}$ values are generally too small; i.e., $\Delta E_{N-\Delta}=$ 222 MeV in FSS and 165 MeV in RGM-H compared with the empirical value of 293 MeV. Since the Δ particle does not appear explicitly in our framework, we have not attempted to fit $\Delta E_{N-\Delta}$ in the present calculation.

III. RESULTS AND DISCUSSIONS

A. Determination of the parameters

In addition to four QM parameters, b, m_{ud}, $\alpha_{\rm S}$, and $\lambda=(m_s/m_{ud})$, we have to determine several meson parameters including $f_1^{\rm S}$, $f_8^{\rm S}$, $\theta_{\rm S}$, $f_1^{\rm PS}$, $f_8^{\rm PS}$, $\theta_{\rm PS}$, and the reduction factor c_δ in the PS-meson spin-spin term. The range of the QM parameters is largely constrained by properties of the ground-state baryons; i.e., generally accepted values are $b=0.5-0.6$ fm, $m_{ud}c^2=300-400$ MeV, and $\lambda\lesssim1.69$. The

strength of the FB interaction α_S usually becomes rather large, $\alpha_S=1-2$, compared to the QCD coupling constant. When the meson contribution is not taken into account, the $N-\Delta$ mass difference is usually used to determine α_S through $\sqrt{2/\pi}\alpha_S(\hbar/m_{ud}cb)^3 m_{ud}c^2=440$ MeV. The value of α_S is determined from this equation in FSS. We hope that the meson parameters do not deviate much from those of the standard OBEP. In particular we hope that the SU_6 relation of Eq. (2.18)

$$f_1^S=\sqrt{6}f_8^S, \quad f_1^{PS}=\frac{\sqrt{6}}{5}f_8^{PS}, \tag{3.1}$$

is not severely violated. One may use the $NN\pi$ coupling constant of the standard OBEP approach in order to determine f_8^{PS}. However, we need a careful consideration to find a relationship between $f_{NN\pi}$ and f_8^{PS}. The use of the Gaussian form factor with $b=0.5-0.6$ fm corresponds to a rather low cutoff mass of about $\sqrt{3}/b\sim 600$ MeV, and brings about a fairly large modification of the Yukawa tail of the direct potentials of Eq. (2.8), even in the asymptotic region. We require that the direct potential for the pion exchange coincides with the OPEP used in the hard-core model at $|\boldsymbol{R}|\to\infty$. This leads us to set

$$f_8^{PS}=f_{NN\pi}^{expt}e^{-\alpha_0/2} \quad \text{with} \quad \alpha_0=\frac{1}{3}(m_\pi b)^2. \tag{3.2}$$

This procedure is equivalent to assuming that the $f_{NN\pi}^{expt}$ used in the hard-core model is the momentum-dependent coupling constant at the pole position $\boldsymbol{q}^2=-m_\pi^2$ [28]. We employ $f_{NN\pi}^{expt}=0.278\,43$ following the Nijmegen model-F [17], which leads to $f_8^{PS}=0.269\,94$ in FSS. We determine the S-meson masses to fit available experimental data for the NN and YN systems, considering that the S mesons are not well-established mesons but some substitutes for more complicated meson-exchange processes like 2π exchange, $\rho-\pi$ exchange, and Δ excitations of nucleons. On the other hand, we use the experimental masses for the PS mesons. Once c_δ is determined in the NN system, then it is used in the YN systems without alteration.

We stress that no one has ever successfully introduced the EMEP both for the S and PS mesons at the quark level even for the NN interaction. For example, in their QM study of the NN interaction Takeuchi *et al.* [6] had to introduce different potentials for each state of ^1E, ^3E, ^1O, and ^3O. Both Zhang *et al.* [12] and the Salamanca group [10] find that the NN phase shift of the $^1S_0$ state is too repulsive, once the $^3S_1$ phase shift is fitted to experiment. The origin of this difficulty lies in the imbalance of the color-magnetic repulsion for the ^1S and ^3S states as discussed in our previous paper [16]: If we properly take into account the effect of the very strong one-pion tensor force compatible with the one in the standard OBEP approach, the color-magnetic repulsion of the NN ^3S state is always too weak compared with that of the ^1S state. The assumption of such a common potential, as given by a flavor-singlet scalar meson, is insufficient to give a full account of the central attraction of the NN ^1S and ^3S states. In order to overcome this difficulty, we introduce the spin-dependent or/and isospin-dependent effect into the framework of our model. Our previous model RGM-F shows that the isospin-dependent effect (i.e., δ meson effect) alone cannot solve this problem, but we need to take two different values for the central reduction factor of the S-meson potentials; $c=0.4212$ for ^3E and ^1O, and $c=0.56$ for ^1E and ^3O states. This effect is taken care of by the EMEP of the η, η' PS mesons and the δ meson in the present approach.

We should also mention the mechanism of introducing the flavor dependence in the EMEP of the ϵ meson. The baryon-meson coupling constants for the direct potentials are obtained from Eq. (2.22) by employing the SU_3 relations of the SU_6 unit vectors, $e^e_{(11)000}$ and $e^m_{(11)000}$, given in Table II of [26]. (Note that the definition of α in [26] is $\alpha=D/(F+D)$, and it corresponds to $1-\alpha$ here.) The ϵ-meson coupling constants are given by setting $\alpha=1$ in

$$f_{NN\epsilon}=f_1^S\cos\theta_S+f_8^S\sin\theta_S\frac{1}{\sqrt{3}}(4\alpha-1),$$

$$f_{\Lambda\Lambda\epsilon}=f_1^S\cos\theta_S+f_8^S\sin\theta_S\frac{2}{\sqrt{3}}(\alpha-1),$$

$$f_{\Sigma\Sigma\epsilon}=f_1^S\cos\theta_S-f_8^S\sin\theta_S\frac{2}{\sqrt{3}}(\alpha-1). \tag{3.3}$$

The coupling constants for the S^* meson are obtained by changing θ_S to $\theta_S-\pi/2$ (with an extra overall sign). We see that the direct potentials for the ΛN and ΣN systems become identical for $\alpha=1$. Under this constraint it is not easy to ensure an appropriate relative strength of the central attraction between ΛN and ΣN channels. In particular the central attraction of the $\Sigma^+ p$ channel is usually too strong, if we fix that of the ΛN channel to fit the low-energy Λp cross sections. We avoid this difficulty in two ways. One is to increase the value of θ_S only for the $\Sigma N(I=3/2)$ channel, and the other is to employ Eq. (3.3) with α being an extra parameter. We call the former model FSS and the latter RGM-H. The latter model does not make a full microscopic treatment for the isoscalar S mesons, ϵ and S^*, but applies the same approximation as used in RGM-F for the evaluation of the spin-flavor-color factors of these mesons. Note that the nonisoscalar mesons, δ and κ, satisfy the SU_6 rule with $\alpha=1$ even in this case.

The procedure used to fix the model parameters of FSS is composed of two steps. The first step is to reproduce the NN phase shifts as well as possible. The second is to optimize the fit to the low-energy YN cross sections by varying those parameters which are insensitive to the NN phase shifts. We first determine f_1^S to reproduce correctly the deuteron binding energy ϵ_d and the spin-singlet scattering length a_s of the np system. These two conditions give two solutions for f_1^S in general, so that f_1^{PS} is varied to yield a unique set under some appropriate value for f_8^S. Since the result is not sensitive to the parameter θ_{PS}, we assume $\theta_{PS}=-23°$ for simplicity. Even if we can reproduce NN S-wave phase shifts in this way, P-wave phase shifts are not usually well reproduced. Thus we select f_8^S and c_δ to obtain a good fit to the S-wave and P-wave phase shifts simultaneously. Since the S^* meson does not contribute too much because of its

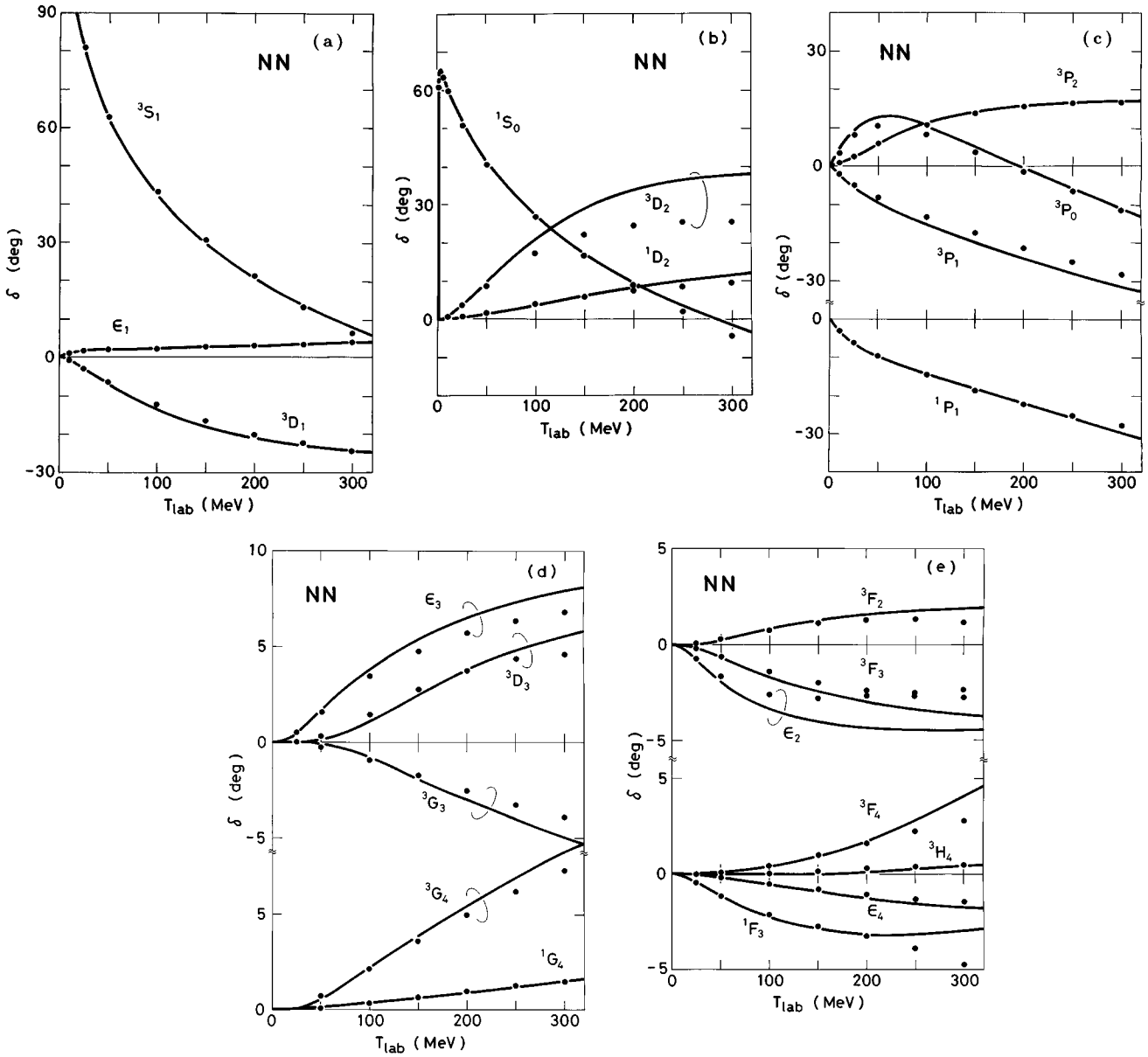

FIG. 1. The NN phase shifts δ and mixing parameters ϵ predicted by FSS as a function of the laboratory energy: (a) δ for $^3S_1$ and $^3D_1$ channels, and ϵ_1, (b) δ for $^1S_0$, $^3D_2$, and $^1D_2$, (c) δ for $^3P_J(J=0,1,2)$ and $^1P_1$, (d) δ for $^3D_3$, $^3G_3$, $^3G_4$, and $^1G_4$, and ϵ_3, (e) δ for $^3F_2$, $^3F_3$, $^1F_3$, $^3F_4$, $^3H_4$, and ϵ_2, ϵ_4. The Coulomb force is neglected. Solid circles denote the recent phase-shift analysis by the Nijmegen group [31] for the np system.

very large mass, we may at first determine θ_S to set f_{NNS*} zero; $\tan\theta_S=(\sqrt{3}f_8^S/f_1^S)$. A small deviation of f_{NNS*} from zero does not impair the nice fit to the NN system. The main effect of changing θ_S through f_{NNS*} lies in adjusting the relative strength of the medium-range attraction between the NN and YN systems. The magnitude of f_8^S is also very important to control this difference. If f_8^S is too small, one cannot get enough suppression of the YN central attraction (see the discussion in [16]). The overall fit to the NN S- and P-wave phase shifts is achieved also by searching for an optimum set for the QM parameters, b and m_{ud}, and less extensively for the S-meson masses, m_ϵ and m_δ.

The next step is to fix θ_S, λ, and m_κ to reproduce the low-energy YN cross-section data and the $\Lambda-\Sigma$ mass difference. If θ_S is changed, f_1^S is readjusted to give the same $f_{NN\epsilon}$ coupling constant through Eq. (3.3). Since this change also affects f_{NNS*}, we can use it to determine θ_S. If f_{NNS*} increases from zero, then θ_S decreases and one can increase the overall attraction in the YN systems, keeping that of the NN system almost unchanged. The difference of ΛN $^1S_0$ and $^3S_1$ phase shifts and the mass difference $\Delta E_{\Lambda-\Sigma}$ are very sensitive to the variation of λ and m_κ. Increasing λ from one and decreasing m_κ both lead to larger $\Delta E_{\Lambda-\Sigma}$ and smaller ΛN cross sections through the less attractive nature of the ΛN $^3S_1$ phase shift. This tendency is not favorable, because Λp cross sections are usually too small if we fit $\Sigma^+ p$ cross sections. We would rather fit the Λp cross sections and reduce the attraction of the $\Sigma^+ p$ system by taking a large value of θ_S only for the $\Sigma N(I=3/2)$ system. In this process we also pay attention to the $\Sigma N(I=1/2)$ $^3S_1$ phase

TABLE III. Quark-model parameters, SU_3 parameters of the EMEP, S-meson masses, and the reduction factor c_δ for FSS and RGM-H models. The parameter α denotes the $F/(F+D)$ ratio for the flavor-octet SU_3 coupling constants. The ϵ mass denoted by ''two-pole'' indicates two-pole approximation, for which m_1c^2 (β_1) and m_2c^2 (β_2) are shown below the table. The meson parameters of the Nijmegen soft-core potential [29] are also shown as NSC for comparison.

	b (fm)	$m_{ud}c^2$ (MeV)	α_S	$\lambda=m_s/m_{ud}$
FSS	0.616	360	2.1742	1.526
RGM-H	0.667	389	2.1680	1.490
	f_1^S	f_8^S	θ_S (deg)	α
FSS	2.89138	1.07509	27.78 [a]	1
RGM-H	2.95388	0.86906	36.018	1.32 [b]
NSC	3.75548	1.27734	40.895	1.28555
	f_1^{PS}	f_8^{PS}	θ_{PS} (deg)	α
FSS	0.21426	0.26994	-23	2/5
RGM-H	0.16118	0.26851	-23	2/5
NSC	0.18455	0.27204	-23	0.355
	$m_\epsilon c^2$ (MeV)	$m_{S*}c^2$ (MeV)	$m_\delta c^2$ (MeV)	$m_\kappa c^2$ (MeV)
FSS	800	1250	970	1145
RGM-H	Two-pole [c]	1250	980	920
NSC	Two-pole [d]	975	980	1000
	c_δ			
FSS	0.381			
RGM-H	0.339			

[a] $\theta_S=65°$ is used in the $\Sigma N(I=3/2)$ channel.
[b] $\alpha=1$ for nonisoscalar mesons.
[c] 487.818 MeV (0.16900) and 1021.14 MeV (0.61302) [28].
[d] 500.45 MeV (0.18719) and 1047.14 MeV (0.60105) [30].

shift, because both the $I=1/2$ and $I=3/2$ phase shifts have a crucial influence on the $\Sigma^- p$ elastic, $\Sigma^- p \to \Sigma^0 n$ charge exchange, and $\Sigma^- p \to \Lambda n$ reaction cross sections.

The procedure to find a parameter set for RGM-H is almost the same as the above except for some small alterations. We employ an additional parameter α to control the relative strength of the ΛN and ΣN attraction. If we increase α from one, the attraction of the YN systems is strongly hindered as a whole. We therefore use the two-pole approximation for the ϵ-meson exchange potential. (See Table I of [28].) We employ the pp data to fit the S- and P-wave phase shifts and the scattering length a_s in the NN system, after incorporating the ''pion-Coulomb'' corrections [28]. We will discuss this Coulomb problem in Secs. III B and III C. The α_S value is also varied to obtain the optimal fit in the NN system.

Table III shows the result of the parameter search. The values of b, m_{ud}, and λ in FSS and RGM-H turn out to be relatively large compared with those in RGM-F. The large value of b may be related to omitting the vector mesons in the present model. If we take b smaller than 0.6 fm, it is not easy to reproduce the NN $^3P_2$ phase shift, even when the other S-wave and P-wave phase shifts are reproduced well. The SU_3 parameters of the EMEP are given together with those of the Nijmegen soft-core potential (NSC) [29]. The $F/(F+D)$ ratio α is not an adjustable parameter, except for the ϵ- and S^*-exchange potentials of RGM-H. The SU_3 parameters of our model are similar to those of NSC. The deviation of the SU_3 coupling constants from the SU_6 relations of Eq. (3.1) is 10 – 60 %. The model FSS uses $\theta_S=65°$ only for the $\Sigma N(I=3/2)$ channel and $\theta_S=27.78°$ otherwise, while RGM-H uses $\alpha=1.32$ for ϵ- and S^*-exchange potentials and $\alpha=1$ for δ- and κ-exchange potentials.

B. NN phase shifts

Figures 1(a)–1(e) compare the np phase shifts predicted by FSS with the recent phase-shift analysis by the Nijmegen group [31]. The $^1P_1$ phase shift and the low-energy behavior of the $^1S_0$ phase shift demonstrate remarkable improvement over the previous RGM-F result [18], owing to the correct treatment of the long-range OPEP tail in the spin-spin term. For the same reason, the phase shifts of higher partial waves with $L=2\sim4$ are also reproduced within an accuracy of 1° to 2° at $T_{lab}=300$ MeV, except for the $^3D_2$ phase shift [see Fig. 1(b)]. The overestimation of this phase shift is 6° at $T_{lab}=150$ MeV and 12° at $T_{lab}=300$ MeV. The tensor and quadratic spin-orbit components originating from the FB tensor term are not sufficient to reduce the too strong one-pion tensor force in this channel. Closer examination of the phase-shift behavior still indicates a couple of insufficient points. First of all, the peak value of the $^3P_0$ phase shift in Fig. 1(c) is about 2° too high, while the $^3P_1$ phase shift is a little too repulsive on the high-energy side. Since the $^3P_2$ phase shift is almost perfectly reproduced, this implies that the LS and tensor forces are slightly too strong and the central attraction is slightly too weak. The mixing parameter ϵ_2 in Fig. 1(e) shows that its absolute value is too large by about 2°. This tendency is already seen in RGM-F (see Fig. 4 of [18]). A similar feature is also seen for ϵ_3 in Fig. 1(d). On the other hand, ϵ_1 and ϵ_4 are almost perfectly reproduced as seen in Figs. 1(a) and 1(e), respectively. We note that the accurate determination of ϵ_1 in the variational technique requires a careful selection of the channel radius r_c because of the very long-range tail of the OPEP. If r_c is too small, the mixing angle ϵ_1 is largely overestimated not only in the low-energy region but also even at $T_{lab}=300$ MeV. We have used $r_c=8$ fm in the present calculation, and the inaccuracy is estimated to be less than 0.2°. Another problem is the behavior of the $^1F_3$ and $^3F_4$ phase shifts in Fig. 1(e) on the high-energy side. They are too attractive in the energy range $T_{lab}>200$ MeV. This tendency seems to be a common feature of the QM approach [6].

For calculating pp phase shifts we have to introduce the ''pion Coulomb corrections'' discussed in [31]. These corrections are necessary since the charge independence is broken at least by the electromagnetic interaction, by the neutral-pion and charged-pion mass difference, and by the neutron and proton mass difference. We use a simple $1/r$-type Coulomb potential between quarks and neglect small corrections induced from the mass difference of the up and down quarks. This difference is important to explain the isospin mass splitting of hadrons, but again plays a minor role in the baryon-baryon interaction since the internal-

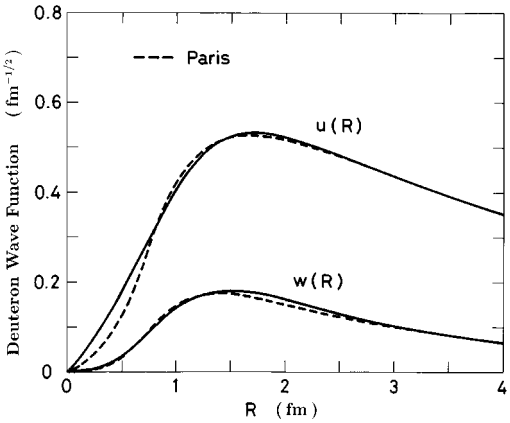

FIG. 2. The S-wave $[u(R)]$ and D-wave $[w(R)]$ deuteron wave functions by FSS as a function of the np distance R. Dashed curves denote those of the Paris group [36].

energy contribution is already subtracted in our RGM formalism [32]. The difference between the charged and neutral pion masses yields a fairly large effect because of the $m_\beta{}^3$ dependence in the pion-exchange direct potential of Eq. (2.8). On the other hand, the effect of the neutron-proton mass difference is rather weak; i.e., less than 0.1% in the empirical reduced mass. Unfortunately these pion Coulomb corrections are not sufficient to reproduce the $np-pp$ difference of the $^1S_0$ phase shift [31]. An extra origin of the charge dependence is clearly necessary to explain the inconsistency of the singlet scattering lengths of the np and pp systems [33]. We have observed these same features in the calculation of the pp phase shifts by FSS. The difference of the np and pp phase shifts for the ^3P_J states is reasonably reproduced only with the pion Coulomb corrections, while the $^1S_0$ phase shift for the pp system is still too repulsive by $2°-3°$, compared with the empirical $np-pp$ difference. This difference is not limited to the low-energy region but continues up to 300 MeV. In the next subsection we will fit the S-wave pp scattering length by slightly decreasing $f_1^{\rm S}$ only for the $^1S_0$ state. The difference up to 2° in the high-energy region still remains even with this modification.

The phase-shift curves of the RGM-H are rather similar to the FSS results. The quality of the fit to the np $(I=0)$ and pp $(I=1)$ phase shift analysis of [31] is a little worse than the fit to np phase shifts by FSS; the difference in the phase shifts sometimes exceeds 2°. The total and differential cross sections and the spin observables calculated by RGM-H seem to be rather good as a whole in comparison with those of FSS, as will be discussed in a forthcoming paper [34].

C. Deuteron properties and effective-range parameters

In this subsection we will discuss the deuteron properties and the low-energy effective-range parameters of the NN system. In principle, the deuteron properties should be derived from the six-quark cluster-model wave function by using electromagnetic currents at the quark level. It is shown in

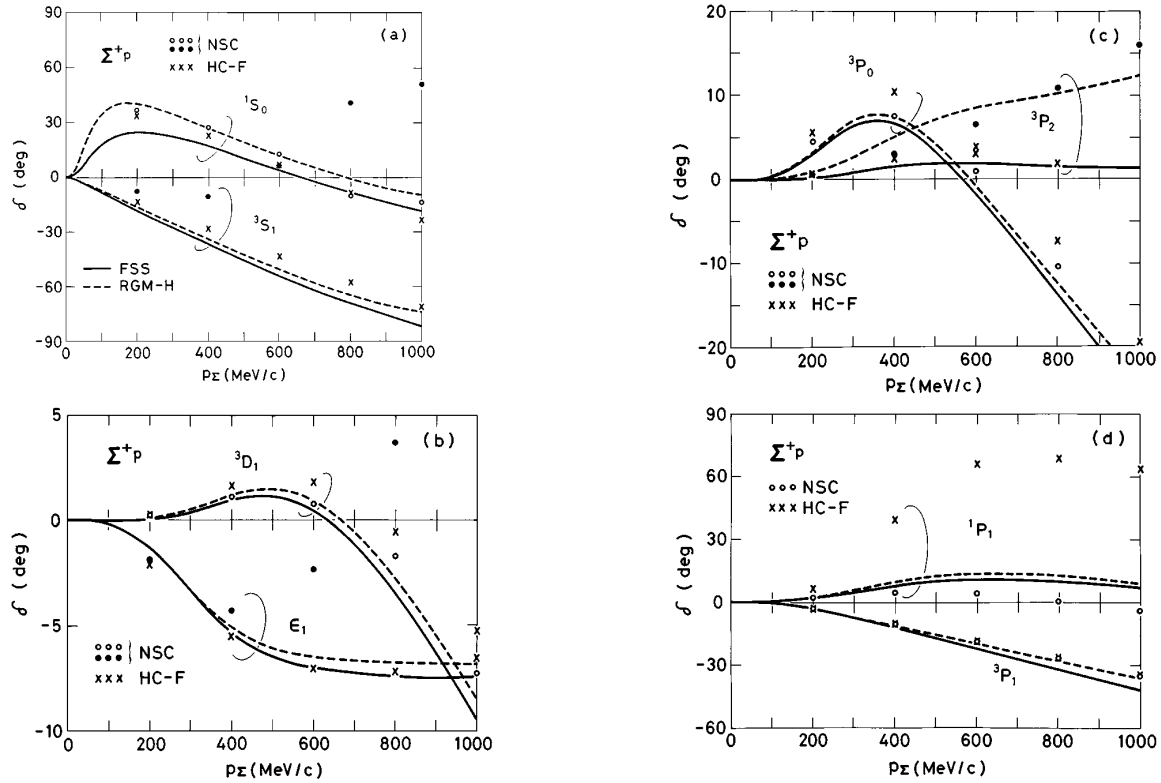

FIG. 3. The Σ^+p phase shifts δ and the mixing parameter ϵ_1 as a function of the incident momentum p_Σ: (a) δ for $^1S_0$ and $^3S_1$ channels, (b) δ for $^3D_1$, and ϵ_1 for the $^3S_1$-$^3D_1$ coupling, (c) δ for $^3P_0$ and $^3P_2$, (d) δ for $^1P_1$ and $^3P_1$. Solid curves denote the FSS result, dashed curves denote RGM-H. Open and solid circles denote predictions by the Nijmegen soft-core potential (NSC) [29], crosses those by the hard-core potential model F (HC-F) [17].

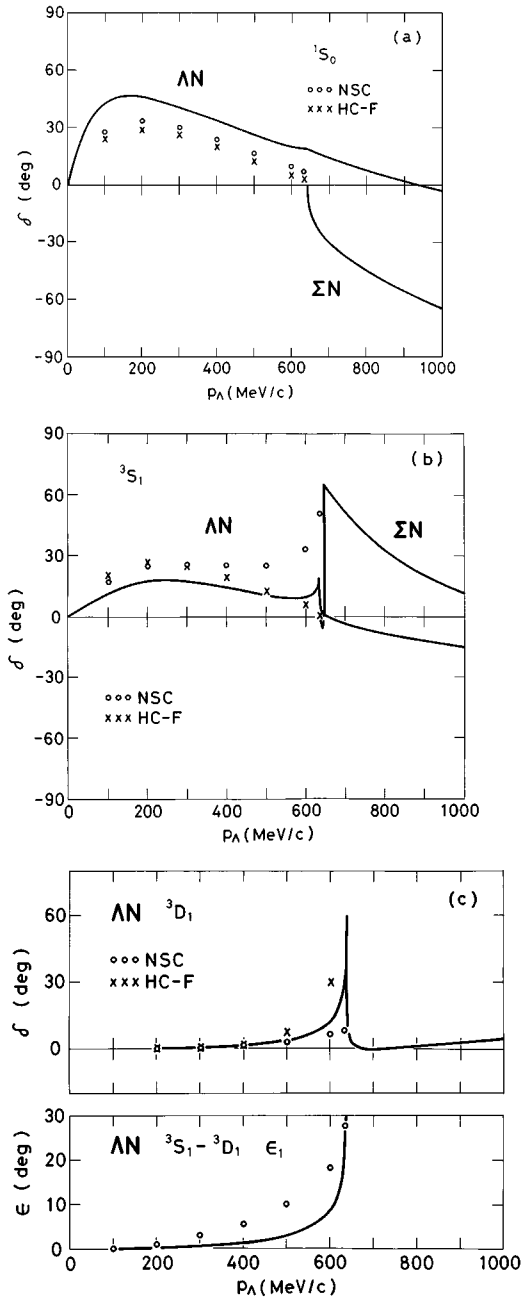

FIG. 4. The ΛN phase shifts δ and the mixing parameter ϵ_1 predicted by FSS as a function of the incident momentum p_Λ: (a) δ for $^1S_0$ channel, (b) δ for $^3S_1$, (c) δ for $^3D_1$, and ϵ_1 for the ΛN $^3S_1$-$^3D_1$ coupling. In (a) and (b), $\Sigma N(I=1/2)$ diagonal phase shifts are also shown above the ΣN threshold at $p_\Lambda=638$ MeV/c. Open circles denote predictions by the Nijmegen soft-core potential (NSC) [29], crosses those by the hard-core potential model-F (HC-F) [17]. The HC-F predictions for ϵ_1 are negative below the ΣN threshold.

[35], however, that a simple renormalized relative wave function, $u_\alpha=(\sqrt{N}\chi)_\alpha$, can be used to calculate them accurately in the conventional method. Here N denotes the normalization kernel of the six-quark system. This is because the contribution of the exchange term is rather small even for the most compact $(0s)^6$ configuration; i.e., the eigenvalue of N is $\mu=1+X_N$ with $X_N=1/9$ for NN ^3E and ^1E states. We follow this approximation to define the relative wave functions of the np system, $u(R)$ (S wave) and $w(R)$ (D wave). We also improve the incorrect asymptotic behavior of the Gaussian trial functions, although we neglect the change of the deuteron binding energy ϵ_d by this modification of the wave function.

TABLE IV. Deuteron properties calculated by RGM-F, FSS, and RGM-H in comparison with the experimental values. The η value is the asymptotic D-state to S-state ratio; $\eta=A_D/A_S$. The magnetic moment is calculated from a simple formula by using the D-state probability P_D.

Model	RGM-F	FSS	RGM-H	Expt.	Ref.
ϵ_d (MeV)	2.274	2.244	2.224	2.224644 ± 0.000046	[37]
P_D (%)	5.391	5.879	4.998		
η	0.0264	0.0272	0.0251	0.0256 ± 0.0004	[39]
$\sqrt{\langle r^2\rangle_d}$ (fm)	1.933	1.966	1.986	1.9635 ± 0.0046	[37]
Q_d (fm^2)	0.2752	0.2845	0.2750	0.2860 ± 0.0015	[40]
μ_d (μ_N)	0.8491	0.8463	0.8513	0.85742	

The deuteron wave function, $u(R)$ and $w(R)$, obtained from FSS is compared in Fig. 2 with the prediction of the Paris potential [36]. The difference of the two models is rather small except that $u(R)$ of the quark model has a slightly larger amplitude in the interior region of $R<1$ fm. Correspondingly the peak positions of $u(R)$ and $w(R)$ are somewhat pushed outside. This can be understood by noting that the short-range repulsion in our quark model originates entirely from the exchange kernel of the color-magnetic interaction. Yamauchi, Yamamoto, and Wakamatsu [35] obtained $u(R)$ and $w(R)$ which are very similar to those of the Paris potential. They have introduced a cutoff function for the theoretical meson-exchange potentials in the interior region, while we use the S-meson potentials with no modification for the whole distance.

Table IV compares various deuteron parameters calculated from the models RGM-F, FSS, and RGM-H. The D-state probability predicted by FSS is 5.9%, and is very close to the result of [35]. The quadrupole moment of [35] is too small by about 2–3 %, while our FSS value agrees well with experiment. Meson-exchange currents involving the exchange of a single pion contribute to the quadrupole moment. If the effect is so large as $\Delta Q_d=0.01$ fm^2 in [38], the FSS overestimates the experimental value. The asymptotic D-state to S-state ratio of the deuteron, $\eta=A_D/A_S$, is 0.0272 in FSS, which is compared to the recent value $\eta=0.0256\pm0.0004$ [39]. The model RGM-H gives the smallest D-state probability, $P_D=5.0\%$, among the three models, and predicts η, Q_d, and the charge rms radius in reasonable range. The magnetic moment is calculated from P_D by using a formula $\mu=(\mu_p+\mu_n)-(3/2)(\mu_p+\mu_n-1/2)P_D$. Precise comparison with the experimental value requires careful estimates of various corrections arising from the meson-exchange current and relativistic effect, etc.

Table V lists the S-wave effective range parameters for the NN system. The scattering length a and the effective-range parameter r for the $^3S_1$ state are well reproduced to within an accuracy of 1 – 2 %, since the ϵ_d is fitted to the experimental value. Underlined values of a for the $^1S_0$ state

TABLE V. The S-wave effective-range parameters for the NN system derived from FSS and RGM-H; a (the scattering length), r (the effective-range parameter), and P (the shape-dependent parameter). The experimental values are from [37]. The underlined figures in the $^1S_0$ state indicate fitted quantities. The coupling constant f_1^S is modified to $f_1^S \times 0.9934$ for the pp $^1S_0$ state in FSS, and to $f_1^S \times 1.010\,35$ for the np $^1S_0$ state in RGM-H. The figures in parentheses are those without the modification.

	Model	a (fm)	r (fm)	P
	FSS	5.41	1.76	-0.009
np $^3S_1$	RGM-H	5.47	1.82	-0.012
	Expt	5.424 ± 0.004	1.759 ± 0.005	
	FSS	$\underline{-23.64}$	2.62	0.028
np $^1S_0$	RGM-H	$\underline{-23.75}$	2.74	0.017
		(-17.23)	(2.83)	(0.016)
	Expt	-23.748 ± 0.010	2.75 ± 0.05	
	FSS	$\underline{-7.81}$	2.63	0.036
pp $^1S_0$		(-8.61)	(2.56)	(0.036)
	RGM-H	$\underline{-7.81}$	2.75	0.023
	Expt	-7.8098 ± 0.0023	2.767 ± 0.010	
	FSS	-16.84	2.72	0.029
nn $^1S_0$	RGM-H	-16.24	2.87	0.018
	Expt	-17.9	2.82	

indicate that they are fitted to experiment. (The small deviation of the FSS value in np $^1S_0$ is due to a poor choice of the variational parameters for the phase-shift calculation.) One has to include at least the pion Coulomb corrections, in order to calculate the spin-singlet S-wave effective range parameters for the pp and nn systems. The values in parentheses in the case of FSS are calculated with these corrections for the pp system. Since the corrected value of -8.61 fm is larger in magnitude than the experimental value, -7.8098 ± 0.0023 [37], our pp potential is found to be too attractive at least for the $^1S_0$ state. In RGM-H the NN parameter search for $^1S_0$ and ^3P_J states is carried out by using the pp data and the pion Coulomb corrections. Then our np potential for the $^1S_0$ state is found to be too repulsive. This is seen from the value in parentheses -17.23 fm for the np scattering length, which is too small in magnitude compared with the empirical value, -23.748 ± 0.010 fm [37]. In both FSS and RGM-H, we definitely need some extra origin of the charge-independence breaking. Here we follow the suggestion of [33], in which this breaking is attributed to the two-pion exchange mechanism and $(\gamma\pi)$ exchanges. In practice, f_1^S is modified to $f_1^S \times 0.9934$ in FSS, and to $f_1^S \times 1.010\,35$ in RGM-H. These are small modifications of order of less than 1%, and applied only to the $^1S_0$ state. The empirical feature of the charge dependence of the $^1S_0$ scattering lengths with respect to the np, pp, and nn systems is reasonably reproduced by this procedure, as is seen in Table V.

D. $\Sigma^+ p$ phase shifts

The phase-shift behavior of the $\Sigma^+ p$ system is depicted in Figs. 3(a) – (d) for FSS (solid curves) and RGM-H (dashed curves). Predictions by the Nijmegen soft-core potential (NSC) (open and closed circles) and the hard-core potential model-F (crosses) are also shown for comparison. The most critical issue of the $\Sigma^+ p$ interaction is the strength of the medium-range central attraction. It is particularly essential to pinpoint the phase-shift rise of the $^1S_0$ state in comparison with that of the pp system. The behavior of the $^1S_0$ phase shifts in Fig. 3(a) shows that the central attraction of RGM-H is stronger than that of RGM-F given in Fig. 5 of [18]. On the other hand, the attraction of FSS is weaker than that of RGM-F. In the ^1E and ^3O states, $\Sigma^+ p$ and pp configurations belong to the same flavor-symmetric states of SU_3 representation $(\lambda\mu)=(22)$. The phase-shift behavior in these states is expected to be very similar as long as the flavor symmetry breaking is not so significant. The ^3P_J phase shifts in Figs. 3(c) and (d) clearly show a competition of the central, LS, and tensor components as seen in the pp system. In particular, the $^3P_2$ phase shift is very sensitive to the strength of the central attraction. The results of RGM-H and RGM-F show a fairly attractive rise up to about 10°, similar to that of the NSC and Nijmegen model-D (HC-D). On the other hand, the FSS predicts a rather moderate rise similar to that of the HC-F. This difference of the $^3P_2$ phase shift is detectable in polarization observables at intermediate energies, as will be discussed in a forthcoming paper [41].

On the other hand, the $^3S_1$ state of the $\Sigma^+ p$ channel belongs to the SU_3 (30) state which is almost forbidden by the effect of the Pauli principle. The eigenvalue of the normalization kernel is $\mu = 2/9$ [16]. The repulsive behavior of the $^3S_1$ phase shift in Fig. 3(a) is a consequence of this kinematical effect arising from the quark structure of the baryons. Since the strength of the repulsion is mainly determined by b, the difference of the phase-shift values by FSS, RGM-H, and RGM-F is not significant in spite of the big difference of the central attraction among these models. The mixing parameter ϵ_1 and $^3D_1$ phase shift in Fig. 3(b) show a behavior entirely different from the NN system.

As noted in our previous publication [18], our quark model predicts a $^1P_1$ phase shift which is substantially different from the Nijmegen hard-core models [see Fig. 3(d)]. The prediction by HC-F shows a very strong resonance behavior around 400 MeV/c, while our quark models always predict a very weak rise of the phase shift as also predicted by NSC. It is very likely that the strong enhancement of the $\Sigma^+ p$ elastic ''total'' cross sections around 450 MeV/c is an artifact of the very singular short-range behavior of the meson-exchange potentials and some specific choice of the hard-core radius in HC-D and HC-F. On the other hand, the NSC phase shift for the $^3S_1$ state shows a broad resonance behavior around 650 MeV/c, which leads to a very small contribution of the $^3S_1$ phase shift to low-energy cross sections.

Finally we summarize in Table VI the S-wave effective range parameters for the $\Sigma^+ p$ system derived from the various models. We find that the $^1S_0$ state of RGM-H is too attractive, while RGM-H and FSS give negative values for r_t consistent with the experimental analysis [44]. A more detailed determination of a_s and a_t is surely necessary.

E. $\Lambda N - \Sigma N (I=1/2)$ system

We here discuss the phase-shift behavior of the $\Lambda N - \Sigma N (I=1/2)$ coupled-channel system. The two models,

TABLE VI. The $\Sigma^+ p$ S-wave effective range parameters derived from RGM-H, FSS, RGM-F, and other models; Nijmegen model-D [42], model-F [17], and Jülich models A and B [43]. The Jülich result is without the Coulomb force. The result of an effective range analysis is taken from [44].

$\Sigma^+ p$	a_s (fm)	r_s (fm)	a_t (fm)	r_t (fm)
RGM-H	-4.21	3.28	0.84	-0.83
FSS	-2.15	4.93	0.95	-0.66
RGM-F	-2.26	2.70	0.79	0.59
Model D	-3.66	3.52	0.34	-7.31
Model F	-3.20	3.87	0.70	-2.11
Model A	-2.26	5.22	-0.76	0.78
Model B	-1.09	10.20	-0.90	-1.24
Expt [44]	-2.42 ± 0.30	3.41 ± 0.30	0.709 ± 0.001	-0.783 ± 0.003

FSS and RGM-H, reproduce the threshold energy of the ΣN channel correctly, unlike our previous model RGM-F. This is a very important ingredient of the analysis, since the coupling feature of these two channels is quite sensitive to this condition. The Coulomb effect is neglected in this subsection.

The S-wave phase shifts of the ΛN channel are displayed in Figs. 4(a) and 4(b) for FSS. The diagonal phase shifts of the ΣN channel are also shown above the ΣN threshold. The phase-shift curves by RGM-H are very similar to those given here. If we compare these with the RGM-F results (Figs. 1 and 2 in [19]), we find that the $^1S_0$ phase shift is more attractive, while the $^3S_1$ phase shift is less attractive. The maximum peak of the S-wave phase shift reaches 47° (46°) for $^1S_0$ and 18° (17°) for $^3S_1$ in FSS (RGM-H). On the other hand, the RGM-F prediction is 29° for $^1S_0$ and 25° for $^3S_1$, which is very similar to the predictions by Nijmegen potentials, NSC (circles) and HC-F (crosses). The $^3D_1$ phase shift and the mixing parameter ϵ_1 in the ΛN channel are depicted in Fig. 3(c). They are very similar to the RGM-F predictions given in Fig. 3 of [19], except that the threshold energy is now at the correct position.

The S-wave effective range parameters given in Table VII show the strong attractive feature of the ΛN $^1S_0$ state compared to the $^3S_1$ state. A main reason for the difference between the present and RGM-F results lies in the different strength of the central attraction induced from the S-meson exchange potentials. In the previous calculation of NN phase shifts by RGM-F, the reduction factor c of the EMEP is $c=0.33$ for the ^3S central phase shift [16], while we need to increase it to $c=0.4212$ when the one-pion tensor force is incorporated [18]. The approximate treatment of spin-flavor-color factors adopted in RGM-F underestimates the role of the one-pion tensor force in the short-range region. In the present full treatment of the exchange kernel, the tensor force of the pion exchange has the same order of magnitude as in the standard OBEP approach. This corresponds to the situation which would be equivalent to taking $c=0.33$ in RGM-F. On the other hand, this improvement of the one-pion tensor force does not affect the ΛN system, since the pions do not contribute in this system. We therefore arrive at the conclusion that the $^3S_1$ phase shift of the ΛN system calculated by FSS and RGM-H should be less attractive than that by RGM-F. Another reason for this big difference in the central attraction is the choice of a larger λ value ~ 1.5 than in RGM-F ($\lambda=1.25$). The increase of λ and the decrease of the κ-meson mass enhance the difference of the attraction between the $^1S_0$ and $^3S_1$ states.

TABLE VII. The ΛN S-wave effective-range parameters derived from RGM-H, FSS, RGM-F, and other models; Nijmegen model D [42], model F [17], and Jülich models A and B [43]. Two results of the effective-range analysis are taken from [45], [46].

ΛN	a_s (fm)	r_s (fm)	a_t (fm)	r_t (fm)
RGM-H	-5.34	2.46	-1.04	4.92
FSS	-5.39	2.26	-1.02	4.20
RGM-F	-2.03	3.05	-1.66	3.26
Model D	-1.90	3.72	-1.96	3.24
Model F	-2.29	3.17	-1.88	3.36
Model D	-1.56	1.43	-1.59	3.16
Model B	-0.56	7.77	-1.91	2.43
Expt [45]	-1.8	2.8	-1.6	3.3
Expt [46]	-2.0	5.0	-2.2	3.5

Another difference from RGM-F in the $^3S_1$ phase shift is that the very sharp steplike behavior in Fig. 2 of [19] has now turned into the cusp structure. This is due to the improvement of the threshold as well as the weaker attraction of the $\Sigma N(I=1/2)$ channel. This is understood from the $\Sigma N(I=1/2)$ $^3S_1$ and $^3D_1$ phase shifts in Fig. 5(a). The solid curves denote the FSS results and the dashed curves RGM-H. Comparing these with the solid curve in Fig. 5 of [19], we find that these models have rather weak central attraction for the $\Sigma N(I=1/2)$ channel. However, the resonance behavior around 100 MeV/c in the $^3S_1$ state is rather sensitive to a small change of the attraction. For example, if the Coulomb attraction is included in FSS, the phase shift changes suddenly in the energy region of less than 100 MeV/c: It starts to decrease slowly from 168°, then suddenly drops down to 70° around 150 MeV/c. This is very similar to the RGM-F result without the Coulomb force, although the phase shift starts from 180° in that case. On the other hand, the Coulomb force does not have such a large effect in RGM-H. The $^3S_1$ resonance in this model has a rather broad structure.

In spite of this rather subtle behavior of the $\Lambda N-\Sigma N$ coupling in the $^3S_1$-$^3D_1$ state, the main characteristics of this coupling is not much different among these three models. This can be seen from the reflection and transmission coefficients illustrated in Fig. 5(b). (See Fig. 6 of [19] for the RGM-F result.) Here the channel indices f and i of η_{fi} are specified as follows: (1) ΛN $^3S_1$, (2) ΛN $^3D_1$, (3) $\Sigma N(I=1/2)$ $^3S_1$, and (4) $\Sigma N(I=1/2)$ $^3D_1$. The magnitude of η_{23} reaches almost 0.8 around 100 MeV/c. This strong coupling between ΛN $^3D_1$ and $\Sigma N(I=1/2)$ $^3S_1$ channels is of course due to the strong one-pion tensor force in this system. Although the magnitude of η_{13} shows some difference among the three models, the largest transmission coefficient at the resonance region is always η_{23}.

Figure 5(a) also shows the $\Sigma N(I=1/2)$ $^1S_0$ phase shift. It is noted that the two-baryon state with $(\lambda\mu)=(11)_s$ includes the $\Sigma N(I=1/2)$ $^1S_0$ component with 90% probability and becomes a forbidden state by the Pauli principle for the

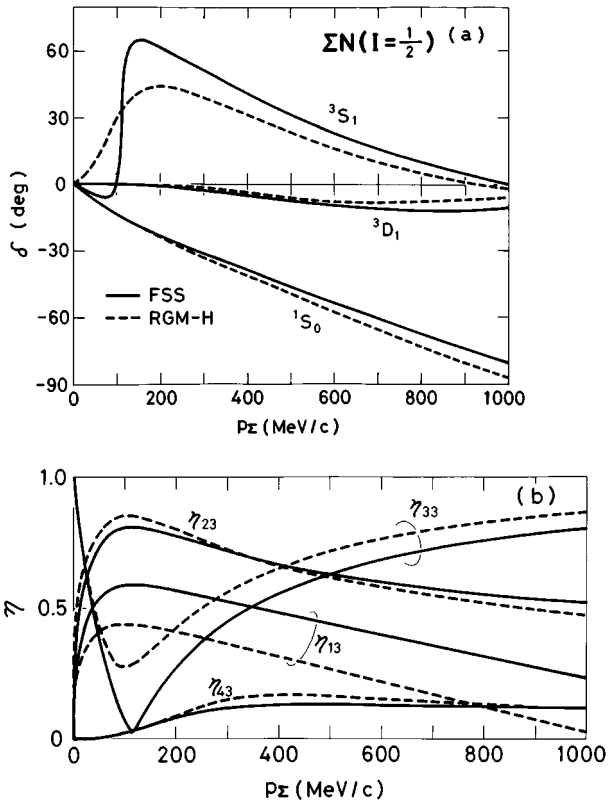

FIG. 5. (a) The $\Sigma N(I=1/2)$ phase shifts for $^3S_1$, $^3D_1$, and $^1S_0$ channels predicted by FSS (solid curves) and by RGM-H (dashed curves) as a function of the incident momentum p_Σ. (b) The reflection and transmission coefficients η_{fi} for $J=1$ even-parity states of the $\Lambda N-\Sigma N(I=1/2)$ system. The incident channel i $(=3)$ and the outgoing channel f are specified by (1) ΛN $^3S_1$, (2) ΛN $^3D_1$, (3) $\Sigma N(I=1/2)$ $^3S_1$, and (4) $\Sigma N(I=1/2)$ $^3D_1$. Solid curves denote the FSS result, dashed curves denote RGM-H.

$(0s)^6$ configuration [19]. The repulsion of this channel is mainly kinematical as in the case of the $\Sigma N(I=3/2)$ $^3S_1$ channel. The effect of the EMEP is rather small in these states.

Next we discuss the $\Lambda N-\Sigma N(I=1/2)$ coupled-channel problem in the $^1P_1$ and $^3P_1$ channels. These two partial waves couple together through the antisymmetric spin-orbit ($LS^{(-)}$) force [21,19]. We here again find that the strength of the central attraction of the $\Sigma N(I=1/2)$ channel influences the coupling features of these four channels. Figures 6(a) and 6(b) show the ΛN phase shifts in the $^3P_1$ and $^1P_1$ channels, respectively, and Fig. 6(c) shows the reflection and transmission coefficients. Here the channel indices are (1) ΛN $^1P_1$, (2) ΛN $^3P_1$, (3) $\Sigma N(I=1/2)$ $^1P_1$, and (4) $\Sigma N(I=1/2)$ $^3P_1$. The $\Sigma N(I=1/2)$ phase shifts calculated with the ΣN channel being an incident channel are displayed in Fig. 7. Table VIII summarizes the resonance behavior in each channel. The large steplike resonance observed in RGM-F [19] in the ΛN $^3P_1$ channel turns into a wavy dispersionlike resonance as seen in Fig. 6(a). On the other hand, the ΛN $^1P_1$ phase shift shows a broad resonance in FSS. However, the RGM-H result shows that this resonance cannot stay in the ΛN channel and goes back to the $\Sigma N(I=1/2)$ $^3P_1$ channel. The resonance feature of RGM-H in Fig. 7 indicates that the phase-shift rise is at most 40° and

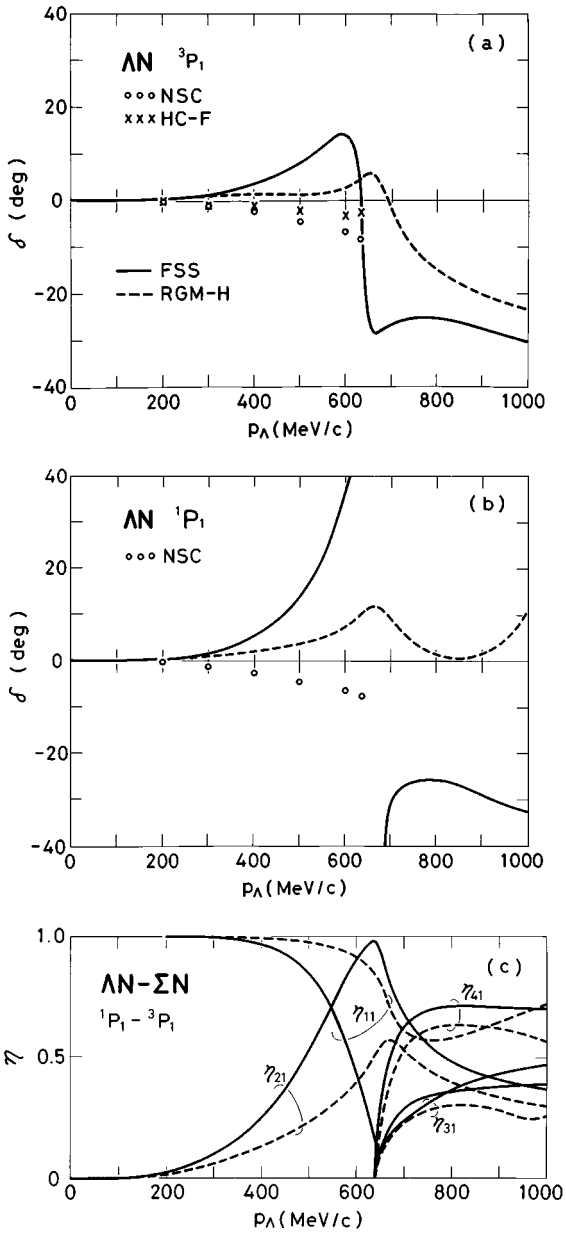

FIG. 6. (a) The Λp phase shifts for the $^3P_1$ channel predicted by FSS (solid curve) and by RGM-H (dashed curve) as a function of the incident momentum p_Λ. The predictions by the Nijmegen soft-core potential (NSC) [29] and those by the hard-core potential model F (HC-F) [17] are also shown by circles and crosses, respectively. (b) The same as (a) but for the $^1P_1$ channel. (c) The reflection and transmission coefficients η_{fi} for $J=1$ odd-parity states of $\Lambda N-\Sigma N(I=1/2)$ system. The channels f and i are specified by (1) ΛN $^1P_1$, (2) ΛN $^3P_1$, (3) $\Sigma N(I=1/2)$ $^1P_1$, and (4) $\Sigma N(I=1/2)$ $^3P_1$. The incident channel is ΛN $^1P_1$. Solid curves denote the FSS result, dashed curves denote RGM-H.

the resonance energy is shifted to the higher-energy side by more than 100 MeV/c, in comparison with the resonance in RGM-F (see the dashed curve in Fig. 13 of [19]). The $^1P_1$ phase shift of RGM-H indicates another prominent resonance structure around 900 MeV/c. All of these features indicate that the central attraction of the $\Sigma N(I=1/2)$ channel in RGM-H is not as strong as in FSS and RGM-F.

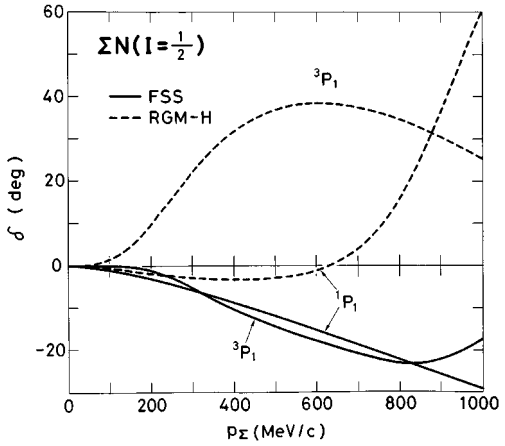

FIG. 7. The $\Sigma N(I=1/2)$ phase shifts for $^3P_1$ and $^1P_1$ channels predicted by FSS (solid curves) and by RGM-H (dashed curves) as a function of the incident momentum p_Σ.

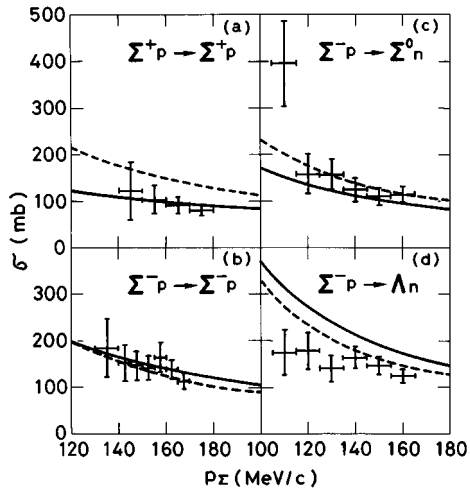

FIG. 8. The low-energy Σ^+p and Σ^-p ''total'' cross sections as a function of the incident momentum p_Σ: (a) Σ^+p elastic, (b) Σ^-p elastic, (c) $\Sigma^-p \to \Sigma^0n$ charge-exchange, (d) $\Sigma^-p \to \Lambda n$ reaction cross sections. Solid curves denote the FSS result, dashed curves denotes RGM-H. The Coulomb force is approximately included. The experimental data are taken from [47] for (a) and (b), and from [48] for (c) and (d).

The strength of the central attraction in the $\Sigma N(I=1/2)$ channel depends on how the flavor dependence to the ϵ-meson exchange potentials is introduced. The flavor dependence introduced in RGM-H through the $F/(F+D)$ ratio results in a common ϵ-meson exchange potential for the Σ^+p and $\Sigma N(I=1/2)$ systems, as far as the dominant direct term is concerned. On the other hand, FSS assumes a large mixing angle θ_S only for the $\Sigma N(I=3/2)$ channel, so that the ϵ-meson exchange potential in the $\Sigma N(I=1/2)$ channel is much stronger than that of the Σ^+p channel. In order to pinpoint the strength of the central attraction in the $\Sigma N(I=1/2)$ channel, more accurate experimental data are needed to determine the effective-range parameters of the Σ^-p scattering.

F. *YN* cross sections

The low-energy scattering and reaction ''total'' cross sections for Σ^+p and Σ^-p systems are compared in Fig. 8 with the experimental data [47,48]. The ''total'' cross sections are calculated by integrating the differential cross sections from $\cos\theta_{\min}=0.5$ to $\cos\theta_{\max}=-0.5$. The solid curves indicate the result by FSS and the dashed curves by RGM-H. The improvement over the RGM-F result [19], especially in the Σ^-p elastic cross sections, is an outcome of the weaker central attraction of the $\Sigma N(I=1/2)$ channel in the present model. On the other hand, $\Sigma^-p \to \Lambda n$ reaction cross sections are overestimated especially in FSS. The agreement of the Σ^+p elastic cross sections in FSS is achieved because the θ_S value is used to fit the data, while RGM-H predicts too large cross sections.

The angular distribution of Σ^+p scattering at $p_\Sigma=170$ MeV/c is compared with the experimental data [47] in Fig. 9(a). A forward rise of the experimental data is reasonably reproduced in FSS, owing to the appreciable contribution of P-wave components. (See Fig. 12 of [18] for comparison.) This feature is also seen in Fig. 9(b), where the angular distribution of Σ^-p elastic scattering at $p_\Sigma=160$ MeV/c is shown with the experimental data [47]. The differential cross sections for $\Sigma^-p \to \Lambda n$ at $p_\Sigma=160$ MeV/c are shown in Fig. 9(c), together with the experimental data [48].

The calculated total cross sections for the Λp scattering are compared with the experimental data [45,46,49] in Fig. 10(a). Since the threshold energy of the ΣN channel is properly reproduced both in FSS (solid curve) and in RGM-H (dashed curve), a cusp structure of the ΛN $^3S_1$ state appears at the incident-momentum of $p_\Lambda=638$ MeV/c. The FSS result shows that the bump structure predicted by RGM-F [19] now spreads out over a wide energy region of $p_\Lambda=500$–800 MeV/c, enhancing the cusp structure. This is the consequence of the P-wave channel-coupling effect with the $\Sigma N(I=1/2)$ channel due to the $LS^{(-)}$ force. On the other hand, RGM-H predicts a rather moderate rise of the cross sections at the cusp region, which is consistent with the experimental data [49]. Figure 10(b) shows calculated $\Lambda p \to \Sigma^0 p$ total cross sections compared with the experimental data [49,50]. Our result appears to favor small cross sections. This may be supported by Fig. 18 of [50], because

TABLE VIII. The resonance behavior of the $\Lambda N-\Sigma N(I=1/2)$ $^1P_1$-$^3P_1$ coupled-channel system in RGM-F, FSS, and RGM-H. The behavior of the ΣN phase shifts δ is also summarized. (See Figs. 6(a), 6(b), and 7, and Figs. 10 and 11 of [19].) The ΣN threshold energy ($\Delta E_{\Lambda-\Sigma}$) is fitted in FSS and RGM-H. The depth of the effective local potentials $V^C_{\Sigma N(I=1/2)}$ in the $^3S_1$ state, obtained from the $\boldsymbol{P}=0$ Wigner transform [16], is shown as a guidance to the strength of central attraction for the $\Sigma N(I=1/2)$ system.

	RGM-F	FSS	RGM-H
$\Delta E_{\Lambda-\Sigma}$ (MeV)	39.11	77.47	77.46
$V^C_{\Sigma N(I=1/2)}$ (MeV)	−38	−24	−18
ΛN $^3P_1$	Steplike	Dispersionlike	Dispersionlike
ΛN $^1P_1$	Dispersionlike	Steplike	Dispersionlike
ΣN $^3P_1$	$\delta<0$	$\delta<0$	$\delta\sim 40°$
ΣN $^1P_1$	$\delta<0$	$\delta<0$	$\delta\sim 0\to 60°$

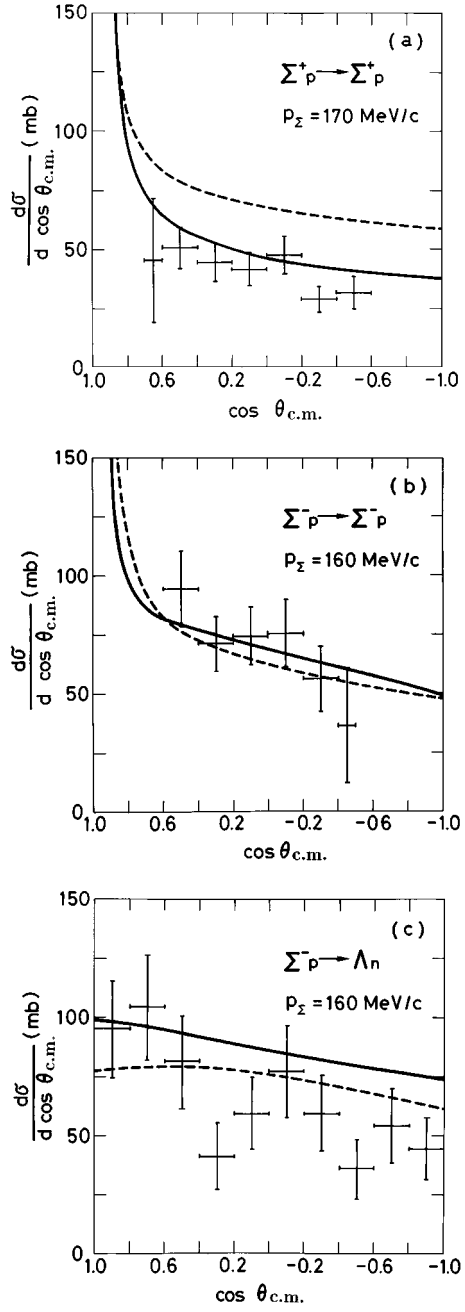

FIG. 9. (a) Comparison of calculated Σ^+p differential cross sections at $p_\Sigma = 170$ MeV/c with the experimental data of [47]. The solid curve denotes the FSS result, the dashed curve denotes RGM-H. (b) The same as (a) but for Σ^-p differential cross sections at $p_\Sigma = 160$ MeV/c. (c) The same as (b) but for $\Sigma^-p \to \Lambda n$ differential cross sections. The experimental data are taken from [48].

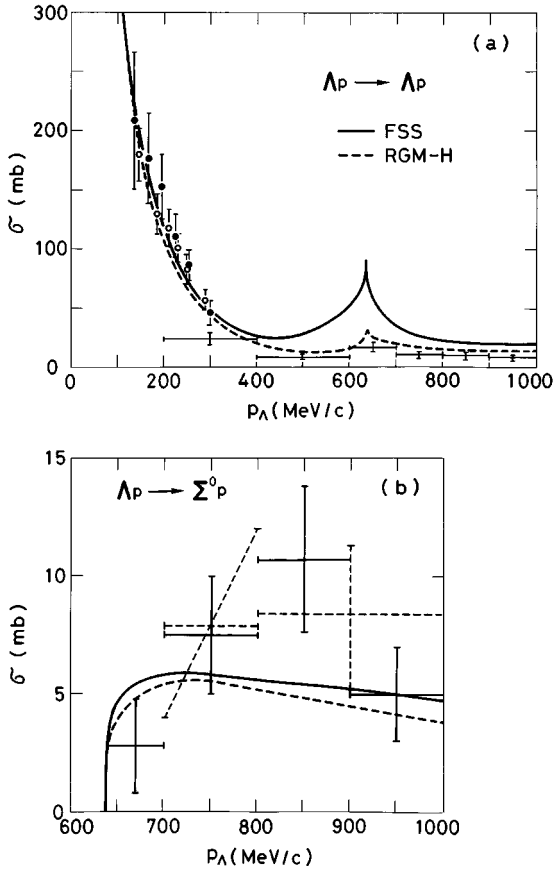

FIG. 10. (a) Comparison of calculated Λp elastic total cross sections with the experimental data of [45] (open circles), [46] (closed circles), and [49] (crosses without circle). The solid curve denotes the FSS result, the dashed curve denotes RGM-H. (b) Calculated $\Lambda p \to \Sigma^0 p$ reaction total cross sections compared with the experimental data of [49] (solid crosses) and [50] (dashed crosses).

much smaller cross sections are predicted if the measured $\Sigma^-p \to \Lambda n$ cross sections are converted into $\Lambda p \to \Sigma^0 p$ cross sections by using the isospin symmetry and the principle of detailed balance.

The energy dependence of Σ^+p and Σ^-p ''total'' cross sections predicted by FSS and RGM-H are displayed in Figs. 11(a)–(d). The Σ^+p cross sections in Fig. 11(a) show no bump structure at the intermediate-energy region (p_Σ=400–600 MeV/c), in contrast to the Nijmegen hard-core models [17,42]. Although RGM-H overestimates the low-energy Σ^+p cross sections, the predictions of FSS and RGM-H at higher energies of more than 400 MeV/c are very similar to each other. This high-energy behavior is shared even in Σ^-p elastic scattering and $\Sigma^-p \to \Sigma^0 n$ charge-exchange reaction cross sections. As is clear in Figs. 11(c) and 11(d), further efforts must be made to get reliable experimental cross sections.

IV. SUMMARY

In the quark-model (QM) study of low-energy hadron phenomena, a basic question is how to incorporate nonperturbative aspects of QCD into the framework. Quark confinement is certainly one of the most important nonperturbative aspects, but it does not seem to play a crucial role in the baryon-baryon interaction except that hadrons are always observed in the color-singlet form. Another important nonperturbative aspect of QCD is the mesonic effect. The most detailed description of the nucleon-nucleon (NN) interaction has been achieved in the last several decades by employing meson-exchange potentials. Since the naive quark model assigning $(3q)$ states to the ground-state baryons does not take into account this effect, a realistic description of the baryon-baryon interaction is only possible if the meson-exchange effect is incorporated into the simple $(3q)$-$(3q)$ formalism.

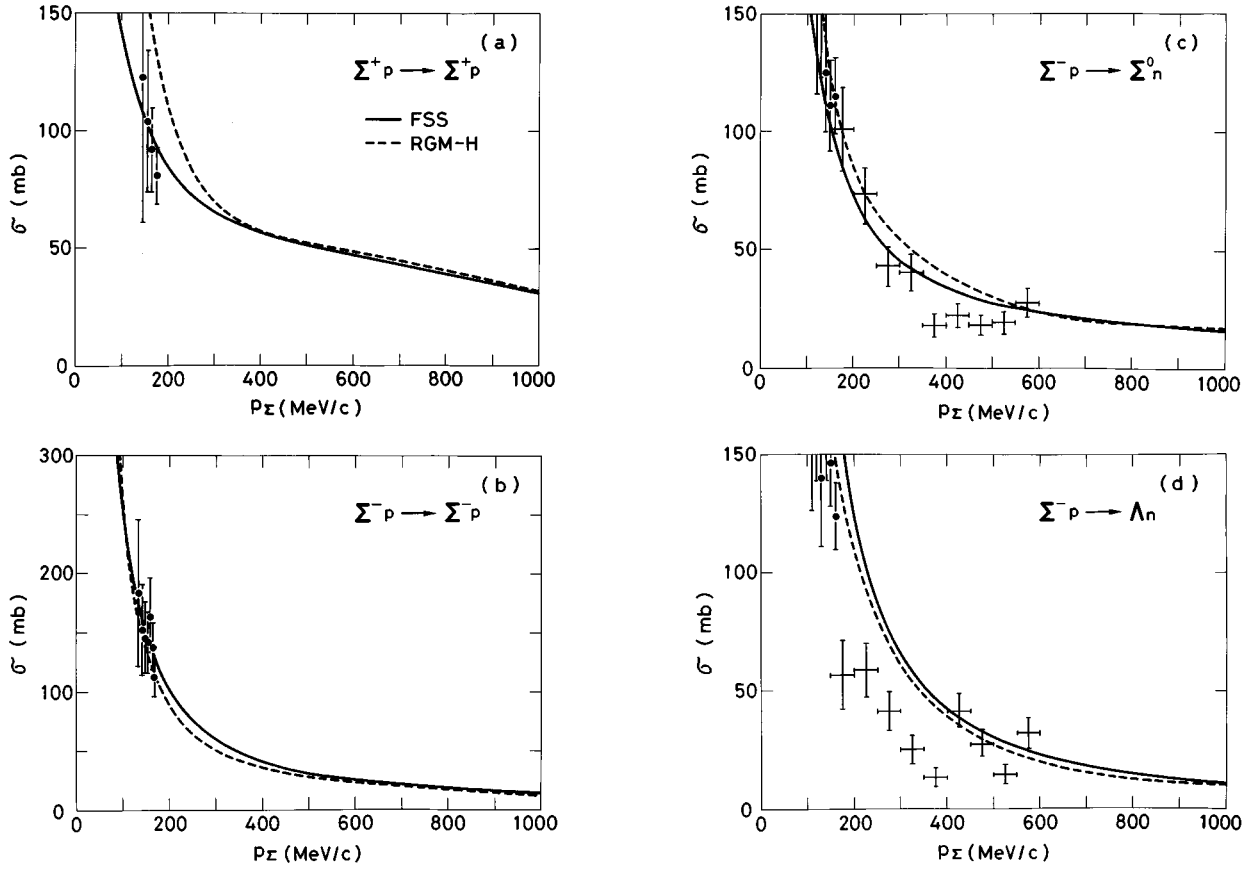

FIG. 11. (a) Comparison of calculated ''total'' cross sections for $\Sigma^+ p$ elastic scattering with the experimental data of [47]. The solid curve denotes the FSS result, dashed curve denotes RGM-H. (b) The same as (a) but for $\Sigma^- p$ elastic scattering. (c) The same as (a) but for $\Sigma^- p \rightarrow \Sigma^0 n$ charge-exchange reaction. The experimental data are taken from [48] (solid circles) and [51] (crosses without circle). (d) The same as (c) but for the $\Sigma^- p \rightarrow \Lambda n$ reaction.

The final goal of this investigation is to understand the NN and hyperon-nucleon (YN) interaction in a consistent framework, thus establishing a natural connection between the QM description of the interaction and the effect of meson-exchange potentials. To achieve this, we first have to answer the following two questions: (i) What kind of difference does the effective meson-exchange potential (EMEP) produce depending on whether it is calculated at the quark level or at the baryon level? (ii) What is the minimum set of mesons indispensably needed? Our quark model is formulated in the resonating-group method (RGM) by employing a QM Hamiltonian consisting of the quadratic confinement potential, the full Fermi-Breit (FB) interaction with explicit quark-mass dependence, and the interquark meson-exchange potentials of the scalar (S) and pseudoscalar (PS) meson nonets. Only the leading term of the central force is introduced for S mesons.

In this study we have improved the following two insufficient points of our previous model RGM-F [16,18,19]; one is that the strength of the medium-range attraction of the EMEP has to be chosen differently depending on the spin-flavor exchange symmetry of the two baryons, and the other is that the threshold energy of the ΣN channel in the $\Lambda N - \Sigma N (I=1/2)$ coupled-channel system is not reproduced well. These difficulties are resolved by evaluating the spin-flavor-color factors explicitly at the quark level. We include the spin-spin and tensor terms from all the PS-meson nonet exchanges. The δ-function-type contact term in the spin-spin part is reduced by a common factor $c_\delta \sim 0.4$. The spin-spin term of η' and η mesons, together with the central term of the δ meson, plays an essential role in the control of the relative strength of the medium-range central attraction of the NN ^1S, ^3S, ^1P, and ^3P states. The explicit evaluation of the spin-flavor-color factors also makes it possible to account for the internal-energy contribution from the EMEP, through which the difference of the threshold energies between ΛN and ΣN channels is calculated to fit the experimental value.

Since the flavor operator of the EMEP for octet mesons is the Gell-Mann matrix, the SU_6 spin-flavor wave functions for the $(3q)$ baryons yields a very strong constraint to the coupling constants of baryon-meson vertices appearing in the direct term of the RGM equation. The SU_3 relations are automatically satisfied in these coupling constants, which is a prominent feature of the SU_6 QM approach to the YN interaction. We can identify the SU_3 parameters for these coupling constants with the SU_3 parameters of the OBEP approach. We write these as f_1, f_8, and θ for each set of the

S and PS mesons. The SU_3 parameter in the OBEP approach, $\alpha=F/(F+D)$, is completely determined to be the pure SU_6 values; $\alpha=1$ for S mesons and $\alpha=2/5$ for PS mesons. The pure electric-type feature of the S-meson exchange potentials turns out to be too strict to obtain a simultaneous fit of the NN phase shifts and the low-energy YN cross sections. We therefore relax this restriction in two ways. In the model called FSS we increase θ_S for S mesons only for the $\Sigma N(I=3/2)$ system in order to decrease the strength of the attraction. On the other hand, RGM-H uses approximate spin-flavor-color factors, as in RGM-F, for the ϵ- and S^*-meson exchange potentials, acquiring the freedom of α for the isoscalar S mesons to control the relative strength of the medium-range attraction between ΛN and ΣN channels.

The QM parameters, the SU_3 parameters of the EMEP, and c_δ are searched for to fit the NN S- and P-wave phase shift values, under the constraint that the deuteron binding energy and the $^1S_0$ scattering length are reproduced. Some parameters, such as the strange to up-down quark mass ratio and the κ-meson mass, are further determined to fit the low-energy cross section data of the YN scattering. Although the harmonic oscillator width parameter and the up-down quark mass turn out to be a little larger than the standard values, the SU_3 parameters of the EMEP have good correspondence to the values of the Nijmegen soft-core potential [29]. We have achieved very good reproduction of the NN phase shifts up to $J=4$ partial waves. The $^1P_1$ phase shift and the low-energy behavior of the $^1S_0$ phase shift are remarkably improved over the RGM-F result [18]. This is mainly due to the correct treatment of the long-range OPEP tail in the spin-spin term. An only exception is the $^3D_2$ phase shift, which is about 10° too attractive at the 300 MeV region. The quadrupole moment of the deuteron is reproduced to within an accuracy of 4%, and the D-state probability is predicted to be 5 – 6%. The effective-range parameters of the NN system are reasonably reproduced. We find that an accurate reproduction of the $^1S_0$ scattering length would require an extra source of the charge-independence breaking in addition to the pion Coulomb corrections [31]. Although the present models do not fit the NN data as well as the OBEP approach, the agreement is satisfactory at least for the purpose of extending the present model to the YN interaction.

The main result of this paper is the simultaneous reproduction of the low-energy Σ^+p, Σ^-p, and Λp cross sections. The overestimation of the Σ^-p elastic cross sections in RGM-F is improved owing to the weaker central attraction of the $\Sigma N(I=1/2)$ channel in FSS and RGM-H. The key point for the present improvement is twofold. The first one is that the reproduction of the NN phase shifts by a unique set of meson parameters has largely reduced the ambiguity of the central attraction in the $\Sigma N(I=1/2)$ channel. Among the three models, RGM-H has the weakest central attraction, FSS the next, and RGM-F the strongest. The other is the reproduction of the ΣN threshold energy in the $\Lambda N - \Sigma N(I=1/2)$ coupled-channel system. The ΛN and $\Sigma N(I=1/2)$ channels are coupled by the one-pion tensor force in the $^3S_1$-$^3D_1$ state and by the antisymmetric spin-orbit ($LS^{(-)}$) force in the $^1P_1$-$^3P_1$ state. The steplike resonance in the ΛN $^3S_1$ state, obtained in RGM-F, is now turned into a cusp structure commonly predicted in the OBEP approach. The dominant coupling between ΛN $^3D_1$ and $\Sigma N(I=1/2)$ $^3S_1$ is crucially influenced by the strength of the central attraction in the $\Sigma N(I=1/2)$ channel. Since the phase-shift rise in the $\Sigma N(I=1/2)$ $^3P_1$ channel is strongly hindered in the present models, the steplike resonance in the Λp $^3P_1$ channel of RGM-F is largely suppressed especially in RGM-H. This resonance appears in the ΛN $^1P_1$ state in FSS. The strong coupling between ΛN and $\Sigma N(I=1/2)$ channels by the $LS^{(-)}$ force enhances the cusp structure at the ΣN threshold. This strong coupling is one of the reasons for too large $\Sigma^-p\to\Lambda n$ cross sections. The Σ^+p cross sections are too large in the low-energy region of $p_\Sigma<300$ MeV in RGM-H. The angular distributions of the differential cross sections for Σ^+p elastic, Σ^-p elastic, and $\Sigma^-p\to\Lambda n$ reaction processes are reasonably well reproduced. In contrast to the Nijmegen hard-core models [17,42] our quark models do not predict any bump structure in the Σ^+p elastic ''total'' cross sections.

A couple of problems still remain to be investigated. First, the central attraction of the Σ^+p channel is still in general too attractive when the total cross sections of Λp elastic scattering are fitted to experiment in the low-energy region. To change θ_S only for the $\Sigma N(I=3/2)$ channel or to change α only for the ϵ and S^* mesons is not completely satisfactory for a consistent understanding of NN and YN interactions. It will be necessary to inquire into the origin of the S-meson exchange in order to clarify the apparent SU_6 symmetry breaking of the S-meson exchange potentials. Second, vector mesons are entirely neglected in the present models. Most important short-range effects of the vector mesons such as the central repulsion and the LS force are expected to be taken into account by the present QM approach, but no one has yet quantified it. The too attractive NN $^3D_2$ phase shift may indicate that the cancellation mechanism between the pion and ρ meson contributions in the tensor force ought to be included in the present framework. The third is that the relative strength of the central attraction between Λp ^1S and ^3S states cannot unambiguously be determined from the present data for the low-energy Λp total cross sections. The ΛN spin-singlet and triplet scattering lengths should satisfy the condition $|a_s|>|a_t|$ in order to reproduce the spin of the ${}^3_\Lambda H$ ground-state [45]. A recent study on this system in the few-body approach [52] may give a definitive answer to this question. Finally, the strength of the central attraction of the $\Sigma N(I=1/2)$ system should be determined more precisely. This strength is crucial to predict correct coupling features of the ΛN and ΣN systems. In particular the resonance behavior of the $\Sigma N(I=1/2)$ $^3P_1$ state is very sensitive to the $^1P_1$ - $^3P_1$ coupling features by the $LS^{(-)}$ force. A preliminary result [41] shows that spin observables are useful to clarify the role of the noncentral forces and to evaluate the adequacy of various models which reproduce the low-energy YN cross sections equally well. Further experiment is needed in order to extend our understanding of the YN interaction to the same level as that of the NN interaction.

ACKNOWLEDGMENTS

The authors would like to thank members of Nuclear Theory Groups of Kyoto and Niigata Universities for useful

discussions. An enlightening discussion with Professor R. Tamagaki was essential for the present work. They also would like to thank the Research Center for Nuclear Physics, Osaka University, for the grant of computer time. This work was supported by the Grant-in-Aid for Scientific Research from the Ministry of Education, Science, and Culture (Nos. 07640397 and 08239203).

APPENDIX: SPIN-FLAVOR-COLOR FACTORS FOR EMEP

Here we show some spin-flavor-color factors for the RGM kernel of EMEP. According to Eq. (2.9), the basic factors $X_{n\mathcal{T}}^{(\Omega)(\lambda\lambda)}$ ($\Omega=$CN, SS, TN) for $w_{ij}^{(00)}=1$ and $w_{ij}^{(11)}=(\lambda_i\lambda_j)$ are given by

$\Omega(\lambda\lambda)=\mathrm{CN}(00)$:

$$X_{0E}^{(\mathrm{CN})(00)}=6,\quad X_{0D_+}^{(\mathrm{CN})(00)}=9,$$

$$X_{1E}^{(\mathrm{CN})(00)}=2X_N,\quad X_{1S}^{(\mathrm{CN})(00)}=X_{1D_+}^{(\mathrm{CN})(00)}=4X_N,$$

$$X_{1D_-}^{(\mathrm{CN})(00)}=X_N,$$

$\Omega(\lambda\lambda)=\mathrm{CN}(11)$:

$$X_{0E}^{(\mathrm{CN})(11)}=-4,\quad X_{0D_+}^{(\mathrm{CN})(11)}=e_{(11)}^{e\dagger}e_{(11)}^{e},$$

$$X_{1E}^{(\mathrm{CN})(11)}=X_{1E}^{(\mathrm{SS})(00)}+\frac{2}{3}X_N,$$

$$X_{1S}^{(\mathrm{CN})(11)}=X_{1S}^{(\mathrm{SS})(00)}+\frac{4}{3}X_N,$$

$$X_{1D_+}^{(\mathrm{CN})(11)}=[X_{1D_+}^{(\mathrm{SS})(00)}+4X_N]P_\sigma\mathcal{P}-\frac{8}{3}X_N,$$

$$X_{1D_-}^{(\mathrm{CN})(11)}=-\left[\,3+\frac{1}{3}(\boldsymbol{\sigma}_1\cdot\boldsymbol{\sigma}_2)\right]-\frac{2}{3}X_N,$$

$\Omega(\lambda\lambda)=\mathrm{SS}(00)$:

$$X_{0E}^{(\mathrm{SS})(00)}=-6,\quad X_{0D_+}^{(\mathrm{SS})(00)}=(\boldsymbol{\sigma}_1\cdot\boldsymbol{\sigma}_2),$$

$$X_{1E}^{(\mathrm{SS})(00)}=-[\,6X_N+X_{1S}^{(\mathrm{SS})(00)}],$$

$$X_{1S}^{(\mathrm{SS})(00)}=\frac{1}{2}\left[e^{e\dagger}e^{e}-\frac{1}{2}(e^{e\dagger}e^{m}+e^{m\dagger}e^{e})\right]+(\boldsymbol{\sigma}_1\cdot\boldsymbol{\sigma}_2)X_{1S}^{(\mathrm{TN})(00)},$$

$$X_{1D_+}^{(\mathrm{SS})(00)}=[\,3+(\boldsymbol{\sigma}_1\cdot\boldsymbol{\sigma}_2)]X_{1D_+}^{(\mathrm{TN})(00)},$$

$$X_{1D_-}^{(\mathrm{SS})(00)}=-\left[\frac{1}{3}e^{e\dagger}e^{e}+X_N\right],$$

$\Omega(\lambda\lambda)=\mathrm{SS}(11)$:

$$X_{0E}^{(\mathrm{SS})(11)}=28,\quad X_{0D_+}^{(\mathrm{SS})(11)}=(\boldsymbol{\sigma}_1\cdot\boldsymbol{\sigma}_2)X_{0D_+}^{(\mathrm{TN})(11)},$$

$$X_{1E}^{(\mathrm{SS})(11)}=6X_N-\frac{5}{3}X_{1E}^{(\mathrm{SS})(00)},$$

$$X_{1S}^{(\mathrm{SS})(11)}=12X_N-\frac{5}{3}X_{1S}^{(\mathrm{SS})(00)},$$

$$X_{1D_+}^{(\mathrm{SS})(11)}=[\,12X_N-X_{1D_+}^{(\mathrm{SS})(00)}]P_\sigma\mathcal{P}-\frac{2}{3}X_{1D_+}^{(\mathrm{SS})(00)},$$

$$X_{1D_-}^{(\mathrm{SS})(11)}=\frac{1}{3}(\boldsymbol{\sigma}_1\cdot\boldsymbol{\sigma}_2)-9-\frac{2}{3}X_{1D_-}^{(\mathrm{SS})(00)},$$

$\Omega(\lambda\lambda)=\mathrm{TN}(00)$:

$$X_{0D_+}^{(\mathrm{TN})(00)}=1,$$

$$X_{1S}^{(\mathrm{TN})(00)}=\frac{1}{6}\left[e^{m\dagger}e^{m}-\frac{1}{2}(e^{e\dagger}e^{m}+e^{m\dagger}e^{e})\right],$$

$$X_{1D_+}^{(\mathrm{TN})(00)}=-\frac{1}{12}[(e^{e\dagger}e^{e}+e^{m\dagger}e^{m})-(e^{e\dagger}e^{m}+e^{m\dagger}e^{e})],$$

$$X_{1D_-}^{(\mathrm{TN})(00)}=-\frac{1}{6}e^{m\dagger}e^{m},$$

$\Omega(\lambda\lambda)=\mathrm{TN}(11)$:

$$X_{0D_+}^{(\mathrm{TN})(11)}=e_{(11)}^{m\dagger}e_{(11)}^{m},$$

$$X_{1S}^{(\mathrm{TN})(11)}=\frac{4}{3}X_{1S}^{(\mathrm{TN})(00)},$$

$$X_{1D_+}^{(\mathrm{TN})(11)}=2X_{1D_+}^{(\mathrm{TN})(00)}\left(\mathcal{P}-\frac{1}{3}\right),$$

$$X_{1D_-}^{(\mathrm{TN})(11)}=\frac{1}{9}e^{m\dagger}e^{m}-\frac{2}{3},\tag{A1}$$

where $e^{e\dagger}e^{e}=e_{(11)}^{e\dagger}e_{(11)}^{e}+6$, $e^{m\dagger}e^{m}=e_{(11)}^{m\dagger}e_{(11)}^{m}+2/3$, $\boldsymbol{\sigma}_i\equiv\boldsymbol{\sigma}_{B_i}$ $(i=1,2)$, and $X_N=-(1/12)[e^{e\dagger}e^{e}+(\boldsymbol{\sigma}_1\cdot\boldsymbol{\sigma}_2)\,e^{m\dagger}e^{m}]$ is the spin-flavor-color factor of the exchange normalization kernel. The factors $X_{nS'}^{(\Omega)(\lambda\lambda)}$ are equal to $X_{nS}^{(\Omega)(\lambda\lambda)}$ in the present case.

The spin-flavor-color factors of the exchange Coulomb kernel are calculated only for pp system. These are employed in place of Eq. (A9) of [18]:

$$X_{1S}^{\mathrm{CL}}=X_{1S'}^{\mathrm{CL}}=-\frac{1}{27}\left[\,4+\frac{7}{9}(\boldsymbol{\sigma}_1\cdot\boldsymbol{\sigma}_2)\right],$$

$$X_{1D_+}^{\mathrm{CL}}=-\frac{1}{27}\left[\,10+\frac{1}{9}(\boldsymbol{\sigma}_1\cdot\boldsymbol{\sigma}_2)\right],$$

$$X_{1D_-}^{\mathrm{CL}}=-\frac{1}{54}\left[\,17+\frac{65}{9}(\boldsymbol{\sigma}_1\cdot\boldsymbol{\sigma}_2)\right].\tag{A2}$$

[1] C. B. Dover and A. Gal, Prog. Part. Nucl. Phys. **12**, 171 (1984); H. Bando, Y. Yamamoto, T. Motoba, K. Ikeda, and T. Yamada, Prog. Theor. Phys. Suppl. **81**, 1 (1985); H. Bando, T. Motoba, and J. Žofka, Int. Mod. Phys. A **21**, 4021 (1990).
[2] F. E. Close, *An Introduction to Quarks and Partons* (Academic, London, 1979).
[3] M. Oka and K. Yazaki, in *Quarks and Nuclei*, edited by W. Weise (World Scientific, Singapore, 1984), p. 489; K. Shimizu, Rep. Prog. Phys. **52**, 1 (1989); C. W. Wong, Phys. Rep. **136**, 1 (1986).
[4] M. Oka and K. Yazaki, Prog. Theor. Phys. **66**, 556 (1981); **66**, 572 (1981).
[5] M. Oka and K. Yazaki, Nucl. Phys. **A402**, 477 (1983).
[6] S. Takeuchi, K. Shimizu, and K. Yazaki, Nucl. Phys. **A504**, 777 (1989).
[7] K. Shimizu, Phys. Lett. **148B**, 418 (1984).
[8] U. Straub, Zhang Zong-Ye, K. Bräuer, Amand Faessler, S.B. Khadkikar, and G. Lübeck, Nucl. Phys. **A483**, 686 (1988); **A508**, 385c (1990).
[9] K. Bräuer, Amand Faessler, F. Fernández, and K. Shimizu, Nucl. Phys. **A507**, 599 (1990).
[10] F. Fernández, A. Valcarce, U. Straub, and A. Faessler, J. Phys. G **19**, 2013 (1993).
[11] A. Valcarce, A. Buchmann, F. Fernández, and Amand Faessler, Phys. Rev. C **50**, 2246 (1994); **51**, 1480 (1995).
[12] Zong-ye Zhang, Amand Faessler, U. Straub, and L. Ya. Glozman, Nucl. Phys. **A578**, 573 (1994).
[13] L. J. Qi, J. H. Zhang, P. N. Shen, Z. Y. Zhang, and Y. W. Yu, Nucl. Phys. **A585**, 693 (1995).
[14] Y. W. Yu, Z. Y. Zhang, P. N. Shen, and L. R. Dai, Phys. Rev. C **52**, 3393 (1995).
[15] Y. Fujiwara, C. Nakamoto, and Y. Suzuki, Phys. Rev. Lett. **76**, 2242 (1996).
[16] C. Nakamoto, Y. Suzuki, and Y. Fujiwara, Prog. Theor. Phys. **94**, 65 (1995).
[17] M. M. Nagels, T. A. Rijken, and J. J. de Swart, Phys. Rev. D **20**, 1633 (1979).
[18] Y. Fujiwara, C. Nakamoto, and Y. Suzuki, Prog. Theor. Phys. **94**, 215 (1995).
[19] Y. Fujiwara, C. Nakamoto, and Y. Suzuki, Prog. Theor. Phys. **94**, 353 (1995).
[20] K. Yazaki, Prog. Part. Nucl. Phys. **24**, 353 (1990).
[21] C. Nakamoto, Y. Suzuki, and Y. Fujiwara, Phys. Lett. B **318**, 587 (1993).
[22] Y. Fujiwara and Y. C. Tang, *Memoirs of the Faculty of Science*, Kyoto University, Series A of Physics, Astrophysics, Geophysics and Chemistry, **39**, No. 1, Article 5 (Faculty of Science, Kyoto University, Kyoto, 1994), p. 91.
[23] Y. Suzuki and K. T. Hecht, Nucl. Phys. **A420**, 525 (1984).
[24] M. Kamimura, Prog. Theor. Phys. Suppl. **62**, 236 (1977).
[25] Y. Fujiwara, Prog. Theor. Phys. Suppl. **91**, 160 (1987).
[26] Y. Fujiwara, Prog. Theor. Phys. **88**, 933 (1992).
[27] G. Q. Liu, M. Swift, A. W. Thomas, and K. Holinde, Nucl. Phys. **A556**, 331 (1993).
[28] V. G. J. Stoks, R. A. M. Klomp, C. P. F. Terheggen, and J. J. de Swart, Phys. Rev. C **49**, 2950 (1994).
[29] P. M. M. Maessen, Th. A. Rijken, and J. J. de Swart, Phys. Rev. C **40**, 2226 (1989).
[30] M. M. Nagels, T. A. Rijken, and J. J. de Swart, Phys. Rev. D **17**, 768 (1978).
[31] V. G. J. Stoks, R. A. M. Klomp, M. C. M. Rentmeester, and J. J. de Swart, Phys. Rev. C **48**, 792 (1993).
[32] Marc Chemtob and Shin Nan Yang, Nucl. Phys. **A420**, 461 (1984).
[33] T. E. O. Ericson and G. A. Miller, Phys. Lett. **132B**, 32 (1983).
[34] T. Fujita, Y. Fujiwara, C. Nakamoto, Y. Suzuki, T. Yamamoto, and R. Tamagaki, Prog. Theor. Phys. **96**, 463 (1996).
[35] Y. Yamauchi, R. Yamamoto, and M. Wakamatsu, Nucl. Phys. **A443**, 628 (1985).
[36] M. Lacombe, B. Loiseau, J. M. Richard, R. Vinh Mau, J. Côté, P. Pirès, and R. de Tourreil, Phys. Rev. C **21**, 861 (1980).
[37] O. Dumbrajs, R. Koch, H. Pilkuhn, G. C. Oades, H. Behrens, J. J. de Swart, and P. Kroll, Nucl. Phys. **B216**, 277 (1983).
[38] L. J. Allen, H. Fiedeldey, and N. J. McGurk, J. Phys. G **4**, 353 (1978).
[39] N. L. Rodning and L. D. Knutson, Phys. Rev. C **41**, 898 (1990).
[40] David M. Bishop and Lap M. Cheung, Phys. Rev. A **20**, 381 (1979).
[41] T. Fujita, Y. Fujiwara, C. Nakamoto, and Y. Suzuki, Prog. Theor. Phys. **96**, 653 (1996).
[42] M. M. Nagels, T. A. Rijken, and J. J. de Swart, Phys. Rev. D **15**, 2547 (1977).
[43] A. Reuber, K. Holinde, and J. Speth, Nucl. Phys. **A570**, 543 (1994).
[44] M. M. Nagels, T. A. Rijken, and J. J. de Swart, Ann. Phys. (N.Y.) **79**, 338 (1973).
[45] G. Alexander, U. Karshon, A. Shapira, G. Yekutieli, R. Engelmann, H. Filthuth, and W. Lughofer, Phys. Rev. **173**, 1452 (1968).
[46] B. Sechi-Zorn, B. Kehoe, J. Twitty, and R. A. Burnstein, Phys. Rev. **175**, 1735 (1968).
[47] F. Eisele, H. Filthuth, W. Föhlisch, V. Hepp, and G. Zech, Phys. Lett. **37B**, 204 (1971).
[48] R. Engelmann, H. Filthuth, V. Hepp, and E. Kluge, Phys. Lett. **21**, 587 (1966).
[49] J. A. Kadyk, G. Alexander, J. H. Chan, P. Gaposchkin, and G. H. Trilling, Nucl. Phys. **B27**, 13 (1971).
[50] J. M. Hauptman, J. A. Kadyk, and G. H. Trilling, Nucl. Phys. **B125**, 29 (1977).
[51] D. Stephen, Ph.D. thesis, University of Massachusetts, 1970 (unpublished).
[52] K. Miyagawa, H. Kamada, W. Glöckle, and V. Stoks, Phys. Rev. C **51**, 2905 (1995).